Article

Allometric rules for mammalian cortical layer 5 neuron biophysics

https://doi.org/10.1038/s41586-021-04072-3

Received: 8 August 2020

Accepted: 29 September 2021

Published online: 10 November 2021

Check for updates

Lou Beaulieu-Laroche[1], Norma J. Brown[1], Marissa Hansen[1], Enrique H. S. Toloza[1,2,3], Jitendra Sharma[4,5], Ziv M. Williams[6], Matthew P. Frosch[7], Garth Rees Cosgrove[8], Sydney S. Cash[9] & Mark T. Harnett[1]✉

The biophysical properties of neurons are the foundation for computation in the brain. Neuronal size is a key determinant of single neuron input–output features and varies substantially across species[1–3]. However, it is unknown whether different species adapt neuronal properties to conserve how single neurons process information[4–7]. Here we characterize layer 5 cortical pyramidal neurons across 10 mammalian species to identify the allometric relationships that govern how neuronal biophysics change with cell size. In 9 of the 10 species, we observe conserved rules that control the conductance of voltage-gated potassium and HCN channels. Species with larger neurons, and therefore a decreased surface-to-volume ratio, exhibit higher membrane ionic conductances. This relationship produces a conserved conductance per unit brain volume. These size-dependent rules result in large but predictable changes in somatic and dendritic integrative properties. Human neurons do not follow these allometric relationships, exhibiting much lower voltage-gated potassium and HCN conductances. Together, our results in layer 5 neurons identify conserved evolutionary principles for neuronal biophysics in mammals as well as notable features of the human cortex.

Input–output properties across species

We systematically assessed the biophysical features of cortical neurons in acute brain slices from adult individuals. In addition to human brain samples obtained from neurosurgical patients at local hospitals[4], we studied nine mammalian species spanning a range of brain sizes and phylogenetic distances to humans (Fig. 1a, b). We used patch-clamp electrophysiology to record from large layer 5 cortical pyramidal neurons (L5), a cell type that is reliably identifiable (see Methods) due to its morphology and electrophysiological features[8]. In all species, we targeted L5 neurons with the thickest dendrites to isolate putative extra-telencephalic neurons, also referred to as thick-tufted or L5B[8,9] (Methods). The depth of the L5 somas varied according to species (Fig. 1d) and matched histologically defined cortical layers (Extended Data Fig. 1). The surface area and depth of L5 somas were correlated ($r = 0.88$; Fig. 1e, f), but not tightly matched. For example, shorter neurons from ferrets and rabbits had somas of comparable sizes to those of human neurons (Fig. 1d–f). This is likely to reflect differences in neuronal densities (Extended Data Table 1), as primates are known to have higher neuronal densities than non-primates of similar sizes[10].

We began our study by evaluating the electrical properties of the soma, which is the point of convergence in the transformation of inputs to outputs. We first confirmed that neurons from all species match prototypical features of thick-tufted L5 pyramidal neurons[8,9], such as prominent voltage sag and resonant impedance profiles (Extended Data Fig. 2), to ensure that neurons of the same class were being compared. Next, we assessed the somatic input–output transformation, which relates injected current to action potential output (Fig. 1g–j). The somatic input resistance varied considerably across species, such that an identical injection of current yielded markedly different voltage deflections (Fig. 1g, i). Firing patterns were also not conserved: high-frequency bursts were common only in select species (Fig. 1h, Extended Data Figs. 3, 4). The heterogeneity we observed among species was notable, given that the transformation from somatic current input to action potential output is thought to be a fundamental kernel of circuit computation.

The vast majority of synaptic contacts are made at dendrites, which provide sophisticated active and passive forms of information processing at the front end of the input–output transformation[11]. We therefore tested whether the variability we observed in somas (Fig. 1) is a cell-wide phenomenon by performing dendritic whole-cell recordings (Fig. 2a, b; owing to limited tissue availability, dendritic recordings were restricted to human, mouse, gerbil, rat, guinea pig and rabbit). Using local current injections, we mapped L5 dendritic properties at various distances from the soma (Fig. 2d–g, Extended Data Figs. 5, 6). Similar to the somatic recordings, current injections led to diverse responses across species, including variable input resistances and spiking behaviour. With regard

[1]McGovern Institute for Brain Research, Department of Brain and Cognitive Sciences, Massachusetts Institute of Technology, Cambridge, MA, USA. [2]Department of Physics, Massachusetts Institute of Technology, Cambridge, MA, USA. [3]Harvard Medical School, Boston, MA, USA. [4]Picower Institute for Learning and Memory, Department of Brain and Cognitive Sciences, Massachusetts Institute of Technology, Cambridge, MA, USA. [5]Martinos Center for Biomedical Imaging, Department of Radiology, Massachusetts General Hospital and Harvard Medical School, Boston, MA, USA. [6]Department of Neurosurgery, Massachusetts General Hospital, Boston, MA, USA. [7]C.S. Kubik Laboratory for Neuropathology, Massachusetts General Hospital, Boston, MA, USA. [8]Department of Neurosurgery, Brigham and Women's Hospital, Boston, MA, USA. [9]Department of Neurology, Harvard Medical School and Massachusetts General Hospital, Boston, MA, USA. ✉e-mail: harnett@mit.edu

to suprathreshold properties, mice, gerbils, guinea pigs and rabbits exhibited large complex dendritic spikes (Fig. 2c) akin to the canonical calcium plateau potentials described in rats[12,13]. However, their detailed characteristics were not conserved across species (Fig. 2g, Extended Data Figs. 6, 7). We observed a distinct suprathreshold behaviour in human dendrites, characterized by small and narrow spikes[4]. Of note, the high input resistances of human dendrites also diverged from other species (Fig. 2e). Overall, this prominent variance in dendritic physiology strongly suggests that heterogeneous integrative properties manifest cell-wide.

Ionic conductance and neuron size

Our mapping of somatic and dendritic input–output properties across species revealed surprising variability. Although morphological changes alone can substantially alter the electrical behaviour of neurons[14], ion channels also strongly shape subcellular operations. We set out to decipher whether changes in ion channel distributions contribute to the heterogeneous features of L5 cortical neurons. We focused our efforts on voltage-gated potassium channels (K_v) and HCN channels owing to their experimental accessibility (large currents under little to no pharmacological isolation) as well as their strong influence on sub- and suprathreshold properties[13,15,16].

We performed outside-out recordings, in which we voltage-clamped small excised patches of membrane at somatic as well as distal and proximal dendritic locations (Fig. 3a–c, Extended Data Fig. 8). Measured currents were converted into conductance densities (Fig. 3e; also see Methods, Extended Data Fig. 9). We then measured the diameter of L5 dendritic compartments using two-photon *z*-stacks of neurons shortly after removing the patch-clamp electrode, enabling estimation of surface area (Fig. 3d). We used distance-dependent surface area estimates to integrate conductance density plots and compute total conductance estimates (Fig. 3g, h). Our analyses revealed that local and total conductance generally increased from the smaller L5 neurons to the larger ones (Fig. 3e, g, h, Extended Data Fig. 8). However, human L5 neurons were outliers with low conductance despite their large size. To quantitatively determine how size relates to conductance, we used allometric relationships to relate parameters across orders of magnitude using logarithmic scales. When predicting the conductance of human L5 neurons based on the other species, we found human neurons to be statistically significant outliers (Fig. 3g, h, Extended Data Fig. 8). These allometric analyses suggest that human L5 neurons have an unexpected biophysical composition for their size.

Our conductance measurements suggest that human L5 neurons are outliers across six species. The tight correlation between the somatic and dendritic conductance ($r = 0.944$; Extended Data Fig. 8l) for the six initial species suggests that conductance increases in a size-dependent fashion along the entire somatodendritic extent of the neurons. We thus extended our total conductance analysis to include four more species for which we could only obtain somatic data (Fig. 3f). With nine species excluding humans, we observed a faithful adherence to an allometric relationship between somatic K_v conductance and somatic surface area (Fig. 3i). Surface area ($R^2 = 0.965$, $P < 10^{-5}$) was a better predictor than soma depth ($R^2 = 0.930$, $P < 10^{-4}$) for somatic K_v conductance, suggesting that the amount of membrane controls ionic conductance densities. Human L5 neurons were again the sole outliers, exhibiting a much lower K_v conductance than predicted (Fig. 3f, i). Together, our ion channel measurements indicate that human L5 neurons have a unique biophysical make-up among the tested species.

To limit the potential confound of disease states associated with our human brain samples, we compared the biophysical properties of neurons from patients with hippocampal sclerosis; tumour; and other conditions, including gliosis and trauma. We found no significant differences in somatic outside-out currents between the three groups (Extended Data Fig. 7). We also directly tested the effect of epileptic

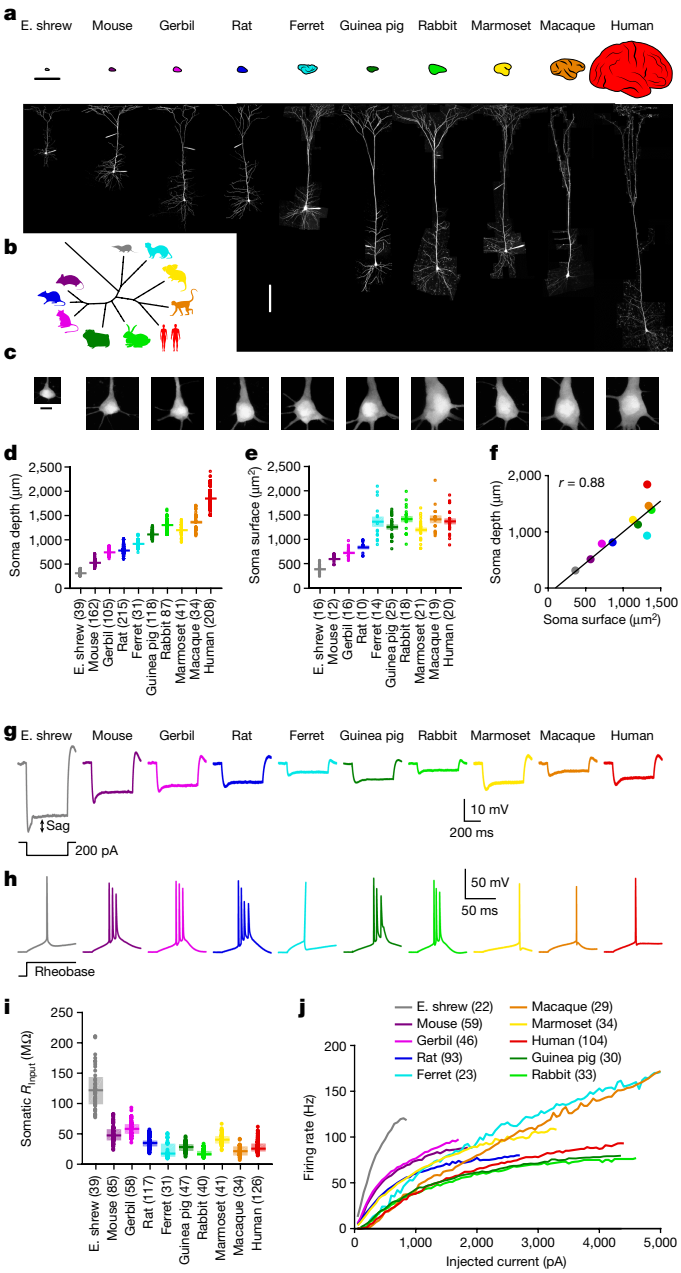

Fig. 1 | Highly variable neuron size and input–output properties across species. a, Two-photon *z*-stack montage images of cortical L5 neurons in 10 mammalian species with corresponding cortex illustration above. See **d** for summary data and sample numbers. E. shrew, Etruscan shrew. Scale bars, 5 cm (top); 200 µm (bottom). **b**, Unrooted phylogenetic tree. **c**, Representative two-photon images of somas of the different species. See **e** for summary data and sample numbers. Scale bar, 10 µm. **d**, **e**, Anatomical measurements across species. Pooled data represent mean ± s.e.m. Sample numbers are indicated in parentheses. **d**, Somatic depth ($P \approx 0$ (one-way ANOVA), $F = 1{,}798$ and 9 degrees of freedom (df)). **e**, Somatic surface area ($P < 10^{-34}$ (one-way ANOVA), $F = 40$ and 9 df). **f**, Relationship between somatic depth and surface area ($R^2 = 0.769$, $P < 0.001$ (linear regression), $F = 26.6$ and 8 df; $n = 10$). **g**, Example somatic voltages in response to subthreshold step current injections. **h**, Same as **g** but for threshold current injections to show spikes. **i**, Somatic input resistance (R_{input}) ($P < 10^{-79}$ (Kruskal–Wallis), $\chi^2 = 399$ and 9 df). Box plots denote the median and 25–75th percentiles. Sample numbers are indicated in parentheses. **j**, Firing rates as a function of injected current. Lines represent population medians. Sample numbers are indicated in parentheses.

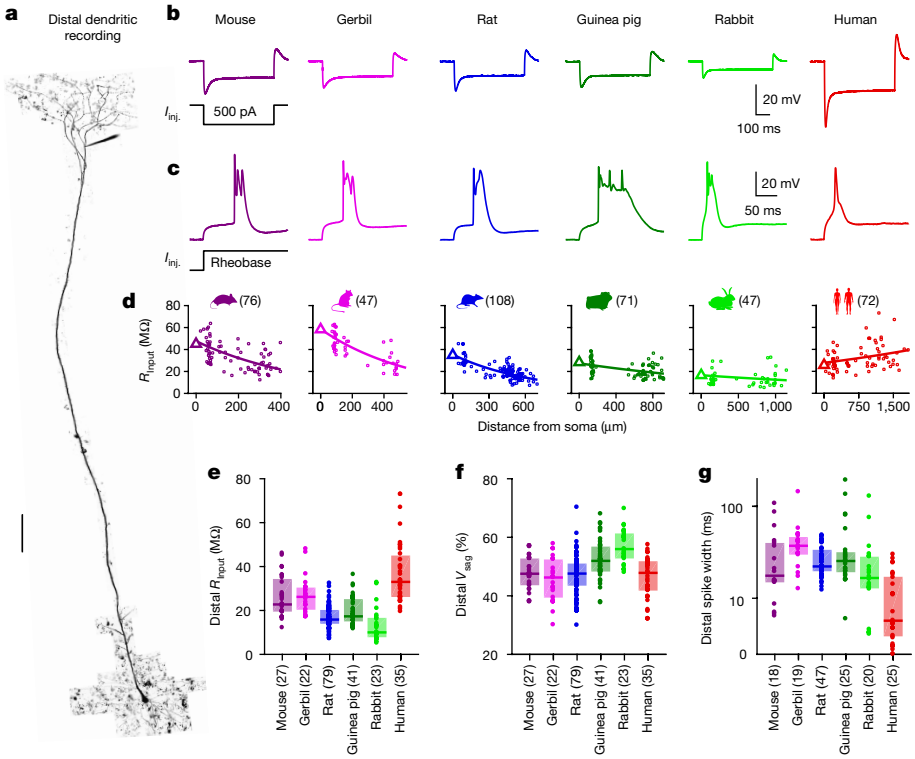

Fig. 2 | Dendritic input–output properties are not conserved across species. a, Two-photon *z*-stack montage image of human neuron with a distal patch-clamp electrode 1,617 µm from soma. Scale bar, 100 µm. **b**, Distal dendritic voltage in response to subthreshold step current injections ($I_{inj.}$). **c**, Same as **b** but for threshold current injections to show dendritic spikes. **d**, Dendritic input resistance as a function of distance from the soma. Triangles are somatic medians, and lines are an exponential fit to the data. Sample numbers are indicated in parentheses. **e**, **f**, Subthreshold properties of distal dendrites. Box plots denote the median and 25–75th percentiles. Sample numbers are indicated in parentheses. **e**, Input resistance ($P < 10^{-20}$ (Kruskal–Wallis), $\chi^2 = 105$ and 5 df). **f**, Voltage sag (V_{sag}) ($P < 10^{-7}$ (Kruskal–Wallis), $\chi^2 = 42$ and 5 df). **g**, Spike width on a log scale of distal dendrites ($P < 10^{-8}$ (Kruskal–Wallis), $\chi^2 = 46$ and 5 df). Box plots denote the median and 25–75th percentiles.

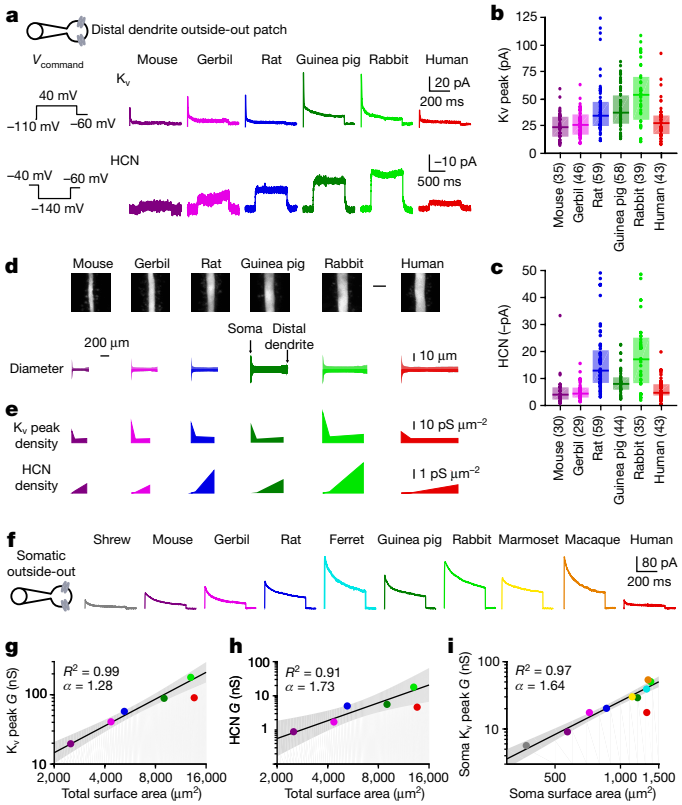

seizures on somatic ionic conductance in rats and found no significant differences (Extended Data Fig. 7). Together, these results suggest that disease aetiology is unlikely to underlie the distinct features of human L5 neurons such as their low conductance.

Conserved conductance per brain volume

We next investigated which other biophysical features can be explained by size by computing the amount of variance explained by allometric relationships with or without human neurons. Most variance in subthreshold properties was explained as long as human L5 neurons

Fig. 3 | Ionic conductance increases with size except in human neurons. **a**, Dendritic outside-out patches were pulled from distal dendrites after obtaining whole-cell recordings. **b**, **c**, Dendritic currents. Box plots denote the median and 25–75th percentiles. Sample numbers are indicated in parentheses. **b**, K_v peak currents ($P < 10^{-8}$ (Kruskal–Wallis), $\chi^2 = 45$ and 5 df). **c**, HCN currents ($P < 10^{-16}$ (Kruskal–Wallis), $\chi^2 = 84$ and 5 df). **d**, Top, two-photon *z*-stack image of distal dendrites. Scale bar, 5 µm. Bottom, distance-dependent median diameter (mouse $n = 12$, gerbil $n = 16$, rat $n = 10$, guinea pig $n = 15$, rabbit $n = 18$, human $n = 20$). **e**, Distance-dependent HCN and K_v peak conductance density. **f**, K_v currents in somatic outside-out patches. Somatic HCN currents were negligible. **g**–**i**, Allometric relationship on a log-log scale for conductance as a function of neuron size. The lines and shaded error bars represent the fit and 95% confidence interval, respectively, of an allometric relationship constructed excluding humans. **g**, Total (soma and dendrite) K_v peak conductance (G) ($P < 10^{-3}$ (linear regression), $F = 193$ and 3 df; $n = 5$). **h**, Total HCN conductance ($P = 0.011$ (linear regression), $F = 31.6$ and 3 df; $n = 5$). **i**, Somatic K_v peak conductance ($P < 10^{-5}$ (linear regression), $F = 192$ and 7 df; $n = 9$).

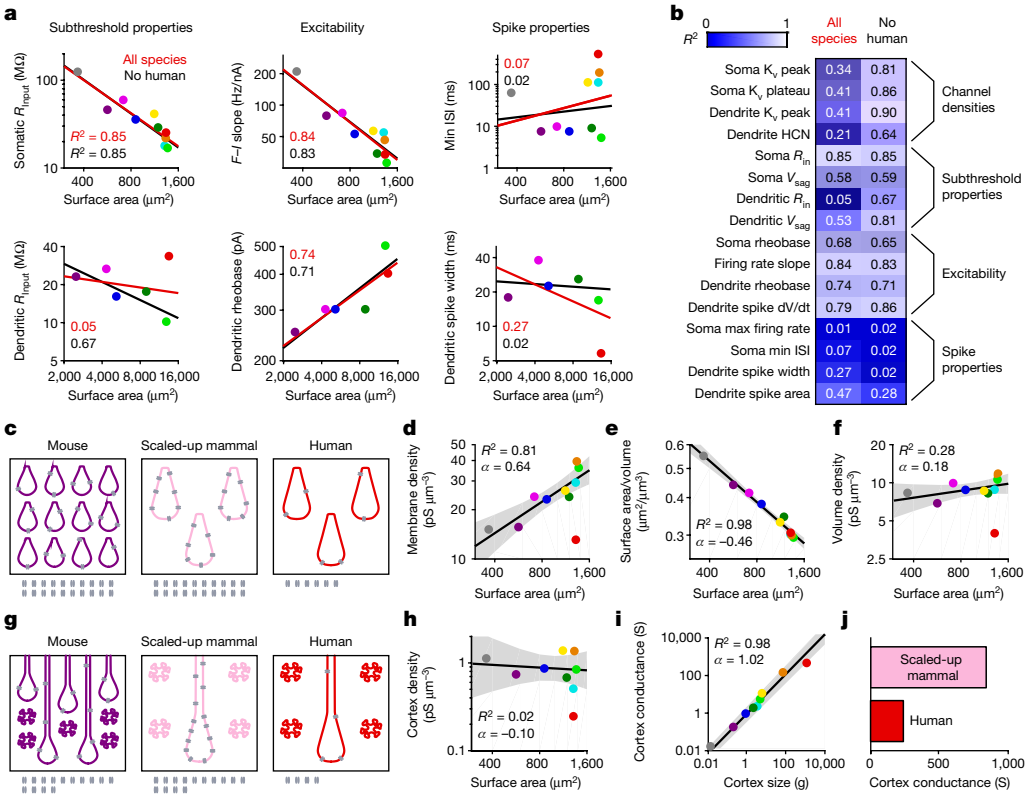

Fig. 4 | Humans are an exception to the allometric relationship that normalizes ionic conductance per brain volume. a, Allometric relationships. *F–I*, firing rate–current; ISI, interspike interval. **b**, Explained variance. **c**, Schematic representation of brain volume occupied by L5 somas. The number of ion channels is indicated at the bottom. **d**–**f**, Allometric relationship on a log-log scale for somatic K_v peak conductance densities in volumes as in **c**. The lines and shaded error bars represent the fit and 95% confidence interval, respectively, of the relationship constructed excluding humans. **d**, Membrane conductance density ($P = 0.001$ (linear regression), $F = 29.2$ and 7 df; $n = 9$). **e**, Surface-to-volume ratio ($P < 10^{-6}$ (linear regression), $F = 318$ and 7 df; $n = 9$). **f**, Volume K_v peak conductance density where the volume is filled with somas ($P = 0.14$ (linear regression), $F = 2.8$ and 7 df; $n = 9$). **g**, Schematic representation of cortex volume with neuronal density from Extended Data Table 1. **h**, **i**, Allometric relationship on a log-log scale for somatic K_v peak conductance densities in volumes as in **g**. The lines and shaded error bars represent the fit and 95% confidence interval, respectively, of a relationship constructed excluding humans. Gerbils were not included because the necessary information was not available in the literature. **h**, Cortex conductance density with accurate neuronal densities ($P = 0.74$ (linear regression), $F = 0.12$ and 6 df; $n = 8$). **i**, Total cortex conductance ($P < 10^{-5}$ (linear regression), $F = 356$ and 6 df; $n = 8$). **j**, Estimated human brain conductance and expected conductance for scaled-up mammalian brain.

were left out. Size also explained most of the variance in somatic and dendritic excitability with or without humans. However, we found that size had very little explanatory power with regard to detailed spike characteristics. High-frequency bursts were only frequent in glires (Extended Data Fig. 4), which include rodents (mouse, gerbil, rat and guinea pig) and lagomorphs (rabbits), suggesting that bursts may be specific to this clade. Furthermore, dendritic spikes had unpredictable shapes and sizes across species (Fig. 2, Extended Data Figs. 6, 7), but this could reflect complex interactions between dendritic length, ion channel densities and somatic coupling[4,12]. Finally, maximal firing rates were not predictable, but the high somatic firing rates of some species (ferret and macaque) could be related to their narrow action potentials (Extended Data Fig. 3). Repeating this analysis by excluding other species (Extended Data Fig. 10) did not yield substantial changes in explained variance, revealing that only human L5 neurons are outliers among the species tested here.

We sought to answer the question of why ionic conductances increase with neuronal size if they do not normalize integrative features. We theorized that the exponential increase in conductance (Fig. 4d) could counteract some other changes that are associated with increasing neuronal size. One direct consequence of a brain with larger neurons is that fewer neurons can fit in the same volume. To examine the effect of neuronal densities on conductance distribution, we approximated a volume composed of L5 somas of different species (Fig. 4c). We also considered a volume filled with scaled-up mammal L5 somas, which are the same size as human neurons but follow the allometric rules that apply to all other species (Fig. 4c). We computed the K_v conductance density per brain volume (Fig. 4c, f) and discovered that it was constant in all tested species besides humans (Fig. 4f). To understand why, we assessed more closely the geometry of neuronal compartments. We found that larger neurons have lower surface-to-volume ratios, meaning that the total membrane area for a specific brain volume is lower (Fig. 4e). Overall, the increase in membrane conductance with size (Fig. 4d) effectively cancels out the decrease in surface-to-volume ratio (Fig. 4e) to maintain a constant conductance per unit volume (Fig. 4f). To test this idea further, we next computed the conductance density in the cortex using neuronal density measurements from the literature (Extended Data Table 1) to account for neuropil (Fig. 4g). Lower neuronal densities were associated with larger L5 soma volumes (Extended Data Fig. 8m), allowing us to use the simplifying assumption that all neurons are L5 neurons. Again, cortical K_v conductance was constant across species (Fig. 4h), leading to a linear increase in cortical conductance with size (Fig. 4i). Humans, however, were outliers at every stage (Fig. 4c–j). With lower ionic conductance than predicted for their size, humans had a lower ion channel conductance per volume than all of the other species, leading to a total cortex conductance four times lower than predicted (Fig. 4i, j, Extended Data Fig. 8). Overall, our analyses suggest that in all tested species except humans, size-dependent rules

for membrane conductances lead to conserved conductance per volume but not to conserved input–output properties.

Discussion

We generated a dataset composed of more than 2,250 patch-clamp recordings (Extended Data Table 2) from a single type of cortical pyramidal neuron across 10 mammalian species, which allowed us to reach two conclusions. First, the biophysical building plan for L5 neurons of different sizes across species does not conserve functional input–output properties but instead normalizes conductance per unit brain volume. Second, human L5 neurons exhibit a distinct biophysical composition compared to other tested species.

The other nine species tested here did not exhibit outlier status according to our analyses in Extended Data Fig. 10. Nevertheless, there were features associated with other species that are worthy of future investigation, such as the fast action potentials in macaque and ferret neurons. Their origin is unclear but our results (Extended Data Fig. 3) are consistent with a previous study that observed very fast action potentials in macaque L5 neurons through extracellular recording[17]. To ensure that the variability in action potential waveforms was not due to differences in brain regions, we compared the firing properties of rat temporal association cortex (TEA) versus M1 and observed only minor changes compared to the large cross-species differences (Extended Data Fig. 3). Work is needed to determine what underlies features like narrow action potentials, as well as other properties across species that were not predictable by size.

Although human cortex adheres to allometric rules regarding its cellular composition and size[10], we find that this is not the case at the biophysical level, unlike all the other mammals we tested. We demonstrate here that the biophysical properties of human L5 neurons are not expected for their size, providing an important locus for future investigations into the human condition. Further work is needed to determine the evolutionary pressures that underlie these distinctive features and their contribution(s) to human brain function.

Online content

Any methods, additional references, Nature Research reporting summaries, source data, extended data, supplementary information, acknowledgements, peer review information; details of author contributions and competing interests; and statements of data and code availability are available at https://doi.org/10.1038/s41586-021-04072-3.

1. Elston, G. N., Benavides-Piccione, R. & DeFelipe, J. The pyramidal cell in cognition: a comparative study in human and monkey. *J. Neurosci.* **21**, RC163 (2001).
2. Mohan, H. et al. Dendritic and axonal architecture of individual pyramidal neurons across layers of adult human neocortex. *Cereb. Cortex* **25**, 4839–4853 (2015).
3. Jacobs, B. et al. Comparative morphology of gigantopyramidal neurons in primary motor cortex across mammals. *J. Comp. Neurol.* **526**, 496–536 (2018).
4. Beaulieu-Laroche, L. et al. Enhanced dendritic compartmentalization in human cortical neurons. *Cell* **175**, 643–651 (2018).
5. Gidon, A. et al. Dendritic action potentials and computation in human layer 2/3 cortical neurons. *Science* **367**, 83–87 (2020).
6. Kalmbach, B. E. et al. h-Channels contribute to divergent intrinsic membrane properties of supragranular pyramidal neurons in human versus mouse cerebral cortex. *Neuron* **100**, 1194–1208 (2018).
7. Verhoog, M. B. et al. Mechanisms underlying the rules for associative plasticity at adult human neocortical synapses. *J. Neurosci.* **33**, 17197–17208 (2013).
8. Hattox, A. M. & Nelson, S. B. Layer V neurons in mouse cortex projecting to different targets have distinct physiological properties. *J. Neurophysiol.* **98**, 3330–3340 (2007).
9. Dembrow, N. C., Chitwood, R. A. & Johnston, D. Projection-specific neuromodulation of medial prefrontal cortex neurons. *J. Neurosci.* **30**, 16922–16937 (2010).
10. Herculano-Houzel, S., Catania, K., Manger, P. R. & Kaas, J. H. Mammalian brains are made of these: a dataset of the numbers and densities of neuronal and nonneuronal cells in the brain of glires, primates, scandentia, eulipotyphlans, afrotherians and artiodactyls, and their relationship with body mass. *Brain Behav. Evol.* **86**, 145–163 (2015).
11. Spruston, N. Pyramidal neurons: dendritic structure and synaptic integration. *Nat. Rev. Neurosci.* **9**, 206–221 (2008).
12. Larkum, M. E., Zhu, J. J. & Sakmann, B. Dendritic mechanisms underlying the coupling of the dendritic with the axonal action potential initiation zone of adult rat layer 5 pyramidal neurons. *J. Physiol.* **533**, 447–466 (2001).
13. Harnett, M. T., Xu, N. L., Magee, J. C. & Williams, S. R. Potassium channels control the interaction between active dendritic integration compartments in layer 5 cortical pyramidal neurons. *Neuron* **79**, 516–529 (2013).
14. Mainen, Z. F. & Sejnowski, T. J. Influence of dendritic structure on firing pattern in model neocortical neurons. *Nature* **382**, 363–366 (1996).
15. Harnett, M. T., Magee, J. C. & Williams, S. R. Distribution and function of HCN channels in the apical dendritic tuft of neocortical pyramidal neurons. *J. Neurosci.* **35**, 1024–1037 (2015).
16. Kole, M. H., Hallermann, S. & Stuart, G. J. Single I_h channels in pyramidal neuron dendrites: properties, distribution, and impact on action potential output. *J. Neurosci.* **26**, 1677–1687 (2006).
17. Vigneswaran, G., Kraskov, A. & Lemon, R. N. Large identified pyramidal cells in macaque motor and premotor cortex exhibit "thin spikes": implications for cell type classification. *J. Neurosci.* **31**, 14235–14242 (2011).

Publisher's note Springer Nature remains neutral with regard to jurisdictional claims in published maps and institutional affiliations.

© The Author(s), under exclusive licence to Springer Nature Limited 2021

Methods

Human and animal models

Species selection. In addition to humans, nine mammalian species were included. Non-mammals were not considered due to a lack of a six-layer cortex and homologous cell types. Mice and rats were included because they are the standard animal models in electrophysiological studies. Marmosets and macaques were included because they are non-human primates and tissue samples were available through local collaborations. Etruscan shrews were included because of their very small brains and neurons. Ferrets were added because they have large neurons but are phylogenetically distant from rodents and primates. Gerbils, guinea pigs and rabbits were selected because they are available through scientific vendors and their neuron size complemented the other species. Owing to varying brain organization and technical consideration, the precise brain regions varied across species but were selected to be the closest analogues to human anterior temporal lobe (see details for individual species below). All animals were used in accordance with the National Institutes of Health (NIH) where applicable and the Massachusetts Institute of Technology Committee on Animal Care guidelines. No sample size calculation was performed. Sample sizes are comparable to or larger than similar studies[4–6]. No blinding or randomization was possible with the study design.

Etruscan shrew. Etruscan shrews (*Suncus etruscus*) were a gift from M. Brecht. Males were housed in groups (up to 3) and used for experimentation at 3–9 months of age.

Mouse. C57BL/6 mice (*Mus musculus*) were purchased from Charles River. Male mice were housed in groups (up to 4) or singly and used for experimentation at 12–28 weeks of age. Mice were housed on a 12–12 dark–light cycle in a room at 20–22 °C and 40–45 % humidity.

Gerbil. Mongolian gerbils (*Meriones unguiculatus*) were purchased from Charles River. Male gerbils were housed in pairs or singly and used for experimentation at 13–17 weeks of age.

Rat. Sprague Dawley rats (*Rattus norvegicus*) were purchased from Charles River. Male and female rats were housed in pairs or singly and used for experimentation at 12–32 weeks of age.

Ferret. Two ferrets (*Mustela putorius furo*) were obtained from the laboratory of C. Walsh and underwent in utero electroporation surgery for an unrelated experiment before being used for our experiments. Six more ferrets were gifted by Tufts University where the only experimental manipulation they would have had is the administration of commercially available human influenza vaccine. Female ferrets were used for experimentation at 9–16 months of age.

Guinea pig. Hartley guinea pigs (*Cavia porcellus*) were purchased from Charles River. Male retired breeders were housed alone and used for experimentation at 27–32 weeks of age.

Rabbit. New Zealand White rabbits (*Oryctolagus cuniculus*) were purchased from Charles River. Male and female rabbits were housed alone and used for experimentation at 25–52 weeks of age.

Marmoset. Brain samples were obtained from 2 male (5 and 7 years old) and 2 female (2 and 6 years old) common marmosets (*Callithrix jacchus*) at Massachusetts Institute of Technology (MIT) that were euthanized as part of experiments unrelated to the current study.

Macaque. Brain samples were obtained from 6 male rhesus macaques (*Macaca mulatta*) at MIT or Harvard Medical School that were euthanized as part of experiments unrelated to the current study (8.5, 9.5, 12, 19 and 21 years old).

Human. Human (*Homo sapiens*) tissue was acquired through collaboration with the Massachusetts General Hospital (MGH) and the Brigham and Women's Hospital (BWH). For MGH, tissue was obtained as 'discarded tissue' from neurosurgical patients in accordance with protocols approved by the Massachusetts General Hospital Internal Review Board (IRB). Patients consent to surgery and a subset of the resected tissue was considered discarded tissue. Under our IRB-approved protocol, such discarded tissue was available for this specific research project for use without explicit patient consent. For BWH, the protocol was approved by the IRB, and patients provided consent prior to the surgery. At both institutions, non-essential samples were extracted by the supervising neuropathologist per protocol.

Patients were male or female adults aged 20–64 years. We report only the sex of the patients because information on their gender identity was not available. Additional patient information is included in Extended Data Table 3. Samples were not allocated to distinct experimental groups and information about the patient was not available until after data acquisition and analysis.

Brain slice preparation

Slicing. Slicing artificial cerebrospinal fluid (aCSF) contained (in mM): sucrose 160, sodium bicarbonate 28, potassium chloride 2.5, sodium phosphate monobasic monohydrate 1.25, calcium chloride 1, magnesium chloride 7.5, glucose 7.25, HEPES 20, sodium pyruvate 3 and sodium ascorbate 3, 295–305 mOsm, pH adjusted to 7.4 with sodium hydroxide. Recovery aCSF contained (in mM): sodium chloride 92, sodium bicarbonate 28.5, potassium chloride 2.5, sodium phosphate monobasic monohydrate 1.2, calcium chloride 2, magnesium chloride 4, glucose 25, HEPES 20, sodium pyruvate 3 and sodium ascorbate 5, 300–310 mOsm, pH adjusted to 7.4 with sodium hydroxide. All solutions were saturated with 95% O_2 and 5% CO_2. Slicing was performed with a vibrating blade microtome in ice-cold slicing aCSF, and 300-µm slices were incubated for around 30 min at 35.5 °C in recovery aCSF. Slices were then stored at around 20 °C until use. Incubation solutions were replaced every 4–8 h.

Etruscan shrew slice preparation. Etruscan shrews were deeply anaesthetized with isoflurane. After decapitation, the head was submerged in ice-cold slicing aCSF. The brain was extracted in about 1 min and placed in slicing aCSF. The two brain hemispheres were either cut apart or kept together. To obtain coronal slices, samples were glued on their frontal surface after performing a blocking cut. Recordings were restricted to the temporal medial cortex[18].

Mouse slice preparation. Mice were deeply anaesthetized with isoflurane. After decapitation, the head was submerged in ice-cold slicing aCSF. The brain was extracted in less than 30 s and placed in slicing aCSF. To obtain slices perpendicular to the surface of the brain, we performed a blocking cut in the frontal cortex of both hemispheres with an approximately 30° yaw angle off the coronal axis. The two hemispheres were separated and glued on their frontal surface. Recordings were restricted to the TEA[2] using the Allen Mouse Brain Atlas as reference (https://mouse.brain-map.org/static/atlas).

Gerbil slice preparation. Gerbils were deeply anaesthetized with isoflurane. After decapitation, the head was submerged in ice-cold slicing aCSF. The brain was extracted in less than 30 s and placed in slicing aCSF. To obtain slices perpendicular to the surface of the brain, we performed a blocking cut in the frontal cortex of both hemispheres with an approximately 35° yaw angle off the coronal axis. The two hemispheres were separated and glued on their frontal surface. Recordings were restricted to the TEA using the same landmarks as for mouse and rat brains.

Some brain extractions were performed in the animal facility. Slicing aCSF was oxygenated for more than 15 min in lab, transported in sealed conditions and used within 15 min. After brain extraction, the brain was transported in sealed conditions for around 5 min before transferring it to freshly oxygenated solution.

Rat slice preparation. Rats were deeply anaesthetized with isoflurane. After decapitation, the head was submerged in ice-cold slicing aCSF. The brain was extracted in less than 30 s and placed in slicing aCSF. To obtain slices perpendicular to the surface of the brain, we performed a blocking cut in the frontal cortex of both hemispheres with an approximately 35° yaw angle off the coronal axis. The two hemispheres were separated and glued on their frontal surface. The pia was completely removed from the cortical surface with fine forceps. Slice preparation with epileptic rats was similar but the extracted brain was transported from MGH to MIT before slicing the same way human tissue was transported. Recordings were restricted to the TEA[2] using the Rat Brain Atlas as reference[19] for all recordings except Extended Data Fig. 3k–m.

Ferret slice preparation. For ferrets euthanized at MIT, anaesthesia was induced with ketamine (25 mg kg^{-1}) and xylazine (2 mg kg^{-1}) intramuscular and supplemented with 5% isoflurane. Following a thoracotomy, ferrets were perfused with slicing aCSF for 1–3 min. Slicing aCSF was oxygenated for more than 15 min in lab, transported in sealed conditions and used within 20 min. After decapitation, the head was submerged in ice-cold slicing aCSF. The brain was extracted in 2–5 min and placed in slicing aCSF. The brain was then transported in sealed conditions for 5–10 min before transferring it to freshly oxygenated solution.

For ferrets euthanized at Harvard Medical School, the ferrets were euthanized with Fatal plus. After a thoracotomy, ferrets were perfused with slicing aCSF for 1–3 min. Slicing aCSF was oxygenated for more than 15 min in the lab, transported in sealed conditions and used within 20 min. After decapitation with scissors, the brain was extracted in 5–10 min and placed in slicing aCSF. The brain was then transported in sealed conditions for 15–25 min before transferring it to freshly oxygenated solution.

Pia and surface blood vessels that would obstruct slicing were removed with forceps. The posterior half of the suprasylvian gyrus[20] was separated from surrounding brain regions and cut in small pieces (around 3 mm × 3 mm) perpendicular (less than 10 degrees off) to the surface of the brain.

Guinea pig slice preparation. Guinea pigs were deeply anaesthetized with isoflurane. After decapitation, the head was submerged in ice-cold slicing aCSF. The brain was extracted in 1–2 min and placed in slicing aCSF. The brain was then transported in sealed conditions for around 5 min before transferring it to freshly oxygenated solution. The pia was completely removed from the cortical surface with fine forceps. The temporal cortex was isolated and cut in small pieces (around 3 mm × 3 mm) perpendicular (less than 10 degrees off) to the surface of the brain.

Rabbit slice preparation. Anaesthesia was induced with ketamine (35 mg kg^{-1}) and xylazine (5 mg kg^{-1}) intramuscular and supplemented with 5% isoflurane. Following a thoracotomy, rabbits were perfused with slicing aCSF for 1–3 min. Slicing aCSF was oxygenated for more than 15 min in the lab, transported in sealed conditions and used within 20 min. After decapitation, the head was submerged in ice-cold slicing aCSF. The brain was extracted in 1–2 min and placed in slicing aCSF. The brain was then transported in sealed conditions for around 10 min before transferring it to freshly oxygenated solution. The pia was completely removed from the cortical surface with fine forceps. The temporal cortex based on this atlas[21] was isolated and cut in small pieces (around 3 mm × 3 mm) perpendicular (less than 10 degrees off) to the surface of the brain.

Marmoset slice preparation. Marmosets were perfused with slicing aCSF for 5–20 min. Slicing aCSF was oxygenated for more than 15 min in the lab, transported in sealed conditions and used within 20 min. The brain was extracted in around 5 min and placed in slicing aCSF. The brain was then transported in sealed conditions for 10–15 min before transferring it to freshly oxygenated solution. A piece of cortex containing inferotemporal gyrus (ITG), superior temporal gyrus (STG) and temporal cortex (TE) was excised based on this atlas[22]. Pia and surface blood vessels that would obstruct slicing were removed with forceps. The sample was then cut in small pieces (around 3 mm × 3 mm) perpendicular (less than 10 degrees off) to the surface of the brain.

Macaque slice preparation. For two macaques, unilateral or bilateral craniotomies were performed under anaesthesia over the temporal lobe. The dura was surgically removed before excising small portions of the temporal lobe. For another macaque, the whole brain was extracted following euthanasia. Tissue was placed in slicing aCSF. For all cases, resected tissue included the temporal cortex between the lateral fissure and the anterior middle temporal sulcus from the tip of the anterior temporal lobe to Bregma −14 mm based on this atlas[23].

Slicing aCSF was oxygenated for more than 15 min in the lab, transported in sealed conditions and used within 20 min. The brain was then transported in sealed conditions for around 5 min before transferring it to freshly oxygenated solution. Pia and surface blood vessels that would obstruct slicing were removed with forceps. The sample was then cut in small pieces (around 3 mm × 3 mm) perpendicular (less than 10 degrees off) to the surface of the brain.

Human slice preparation. Resected human tissue was considered discarded tissue after being examined by neuropathologists whose main objective was to ensure that there was adequate tissue for diagnostic purposes. The neocortical tissue was obtained from the lateral anterior temporal lobe (middle and inferior temporal gyri) in patients undergoing resection of the temporal lobe including mesial structures for medically intractable epilepsy. The neocortical tissue displayed no known abnormalities at the level of MRI scans, gross inspection and subsequent microscopic examination as part of the standard neuropathologic assessment of the tissue. Patients undergoing resective surgery were primarily maintained under general anaesthesia with propofol and remifentanil or sufentanil. Some cases used inhaled anaesthetics, such as isoflurane or sevoflurane. For induction of general anaesthesia, paralytic agents including rocuronium or succinylcholine as well as fentanyl were typically used. Resection usually occurred within 90 min of the start of the procedure.

After resection, tissue was placed within around 180 s in ice-cold slicing artificial aCSF. Samples were transported in sealed conditions for 15–35 min before being transferred to freshly oxygenated solution. Pia and surface blood vessels that would obstruct slicing were removed with forceps and samples were cut in small pieces (around 3 mm × 3 mm) perpendicular (less than 5 degrees off) to the surface of the brain.

Epileptic rat preparation

Rats were implanted with a cannula and monopolar depth electrodes targeted to the hippocampus, as well as four skull screw electrodes (one posterior to lambda, one over the right frontal lobe, one over the left parietal lobe and one over the right parietal lobe). An unconnected anchor screw was placed over the left frontal lobe for implant stability. All electrodes were covered in dental cement and connected to our recording system using a PlasticsOne 6 channel connector.

Epilepsy was induced by administration of 200 ng kainic acid solution (1 mg ml^{-1} of kainic acid in 10× phosphate-buffered saline (PBS)) into the hippocampus via the cannula while the rat was awake using a syringe pump connected to an injector needle. The needle was left in place for 30 s to allow proper diffusion and limit backflow of the

solution. This would induce status epilepticus which was allowed to proceed for at most 2 h before being halted with 5 mg kg^{-1} diazepam. Rats were administered an NSAID (non-steroidal anti-inflammatory drug) (carprofen, 5 mg kg^{-1}) daily for three days after the induction procedure. Electroencephalograms (EEGs) were monitored continuously to check for the onset of spontaneous focal seizures. Rats were euthanized and used for electrophysiological recordings five days after they experienced spontaneous focal seizures.

Patch-clamp recording

Patch-clamp recordings were performed from the soma and apical dendrites of pyramidal neurons at 34–36 °C in recording aCSF containing (in mM): sodium chloride 120, potassium chloride 3, sodium bicarbonate 25, sodium phosphate monobasic monohydrate 1.25, calcium chloride 1.2, magnesium chloride 1.2, glucose 11, sodium pyruvate 3 and sodium ascorbate 1, 302–305 mOsm, saturated with 95% O_2 and 5% CO_2.

Whole-cell current-clamp recordings were performed with an Axopatch 200B, MultiClamp 700b or a Dagan BVC-700A amplifier with series resistance fully balanced. Experiments were performed at the resting membrane potential. Patch pipettes from thick-wall glass (1.5 outer diameter, 0.75 inner diameter) had resistances ranging from 3 to 15 MΩ, and capacitance was fully neutralized prior to break in. Series resistances ranged from 5 to 30 MΩ. The intracellular solution contained (in mM): potassium gluconate 134, potassium chloride 6, HEPES 10, sodium chloride 4, adenosine 5′-triphosphate magnesium 4, guanosine 5′-triphosphate sodium 3, phosphocreatine di (tris) 14 and 0.1 Alexa 488. Liquid junction potential was not corrected for. Current and voltage signals were filtered at 10 kHz and acquired at 20 kHz.

Outside-out (8–13 MΩ pipettes with thick-wall glass) recordings were performed with an Axopatch 200B or a MultiClamp 700b amplifier. For a subset of recordings, the formation of an outside-out patch was confirmed under two-photon imaging (lack of cytoplasmic bridge). Nucleated patch (8–13 MΩ pipettes with thick-wall glass) recordings were performed with an Axopatch 200B or a MultiClamp 700b amplifier. For double nucleated patch experiments, the voltage-clamp amplifier was an Axopatch 200B and the current-clamp amplifier was a Dagan BVC-700A amplifier. Voltage-clamp recordings had series resistance and whole-cell capacitance predicted and compensated >90% and lag <10 μs to effectively command voltage (Extended Data Fig. 9). The nucleus was sucked into the pipette, the pipette was withdrawn and the formation of an excised patch was confirmed under two-photon imaging (lack of cytoplasmic bridge). To record HCN channels, the voltage was stepped to −140 mV for 1,000 ms followed by −60 mV for 1,000 ms from a rest potential of −40 mV[15]. The protocol was interleaved with 4 1/10 scaled protocol for leak subtraction. To record voltage-gated potassium channels, the voltage was stepped to −110 mV for 500 ms followed by +40 mV for 400 ms from a rest potential of −60 mV[13]. The protocol was interleaved with 4 1/10 scaled protocol for leak subtraction. Current signals were filtered at 10 kHz and acquired at 20 kHz. Channel measurements were performed at physiological temperature unlike previous measurements of HCN and K_v in L5 neurons[13,15,24].

For all experiments except Extended Data Fig. 3h–j, we recorded from large L5 pyramids with thick apical dendrites reaching L1[25]. As in previous rodent research, dendritic recordings from unlabelled cells were strongly biased towards thick apical dendrites that reliably originate from large L5 somas. In all species, we targeted the thickest dendrites and biggest L5 somas to isolate putative L5B neurons, also referred to as 'extra-telencephalic' or ET[4,8,9,13,15,26,27].

Two-photon imaging

A multiphoton microscope system with a Mai-Tai DeepSee laser was used to image Alexa 488 at 920 nm or Alexa 594 at 880 nm (separated via dichroic mirrors to independent sets of GaAsP photosensor modules). Another photosensor module was used to collect transmitted-light Dodt gradient images. Laser beam intensity was independently controlled with electro-optical modulators. For some recordings, two-photon imaging was used to target a second location following initial somatic or dendritic recording.

Compartmental modelling

We use a biophysical model of a rat L5 neuron to test the validity of our conductance and outside-out surface areas. Simulations were performed in NEURON v.7.8.2[28]. We used a previously published rat neocortical L5 pyramidal neuron morphology and removed the axon[29]. We implemented the three conductances (HCN, K_v peak, and K_v plateau) on the basis of our measurements (Fig. 3). Leak conductance (reversal −92 mV) was set to 2 pS μm^{-2} in the soma and basal dendrites, 1.54 pS μm^{-2} in apical dendrites and 2.91 pS μm^{-2} in the tuft. Axial resistance was set to 100 Ω*cm in the soma, 100 Ω*cm in the basal dendrites, 250 Ω*cm in the apical dendrites, and 25 Ω*cm in the tuft. Specific membrane capacitance was set to 1 μF cm^{-2} in the soma, 1 μF cm^{-2} in the basal dendrites, 2 μF cm^{-2} in the apical dendrites and 1 μF cm^{-2} in the tuft. Current injection and voltage measurements were simulated at the soma and 520 μm from the soma (distal measurement). Outside-out patches were simulated as spherical compartments with surface areas of 50 μm (Extended Data Fig. 9); and all command voltage protocols were matched to the experimental protocols. All simulations were conducted at 37 °C.

Nissl staining

Shrews, gerbils, mice, rats, ferrets, guinea pigs, rabbits and marmosets were anaesthetized as described above and perfused transcardially with PBS and 4% paraformaldehyde (PFA) in PBS. Whole brains or sections containing the regions of interests were then placed in 4% PFA at 4 °C for 24 h. Macaque and human brain samples were resected under anaesthesia and placed directly in 4% PFA at 4 °C for 24 h. Brain samples were then transferred to PBS at 4 °C until slicing. Brain samples were dissected and tissue blocks were mounted on the vibratome stage in the same manner as samples used for electrophysiological recordings. Particular attention was paid to the angle of slicing to allow for proper comparisons. Slices of 50–60 μm were prepared and transferred to 10% formalin for 10 days. Brain slices were mounted on targeting molecule polysine-coated slides and dried for 2–3 weeks. They were first cleaned with xylene, dehydrated with 100% ethanol, defatted with chloroform (1:1 ratio dilution with 100% ethanol) and rehydrated before staining.

For reliable stains of Nissl bodies and a better visualization of cell bodies, a 0.025% buffered acid thionin stain was used[30,31]. First, 1% thionin was dissolved in distilled water and filtered. Sodium acetate and acetic acid solution were then added and pH adjusted to 5.1–5.5. Thionin buffer solution was kept in dark, maintained under agitation, and the temperature was kept at 37 °C before use. Brain slices were placed in thionin buffer solution for 2–5 min before being rinsed in distilled water to remove excessive dyes. Further colour differentiation was performed with 70% ethanol with acetic acid until the desirable colour and intensity were obtained. To reduce the speed of differentiation, brain slices were transferred to 95% ethanol, and went through the dehydration processes again. Finally, brain slices were cleared in xylene before being covered with DPX and a coverslip. Slices were imaged at 2.5× and 10× with a Zeiss LSM 900.

Conductance density estimation

We devised methods to estimate the membrane area of our outside-out patches. For outside-out surface area, we first used the nucleated patch technique to determine the current per unit area of the somatic membrane of rat neurons (Extended Data Fig. 9). After calibration, we sampled outside-out patches from the same compartment and estimated an outside-out surface area of 50.42 μm^2 (Extended Data Fig. 9). Although our estimate is larger than a prior estimate using capacitive measurements[32], it is worth noting that the specific value used here does not affect cross-species conductance comparisons, which are all relative.

Using the reversal potentials of the channels[15,24], outside-out measurements were effectively converted into conductance densities (Fig. 3e). We validated that our conductance estimates were reasonable using a morphologically realistic biophysical model (Extended Data Fig. 9).

Quantification and statistical analysis

Analysis of voltage and current waveforms was performed using MATLAB codes performing the operations detailed below. Signals were low-pass-filtered at 2.5 kHz for outside-out recordings and nucleated patch recordings. Outside-out recording traces were low-pass-filtered at 100 Hz for display in figures. Input resistance was calculated from the slope of the *I*–*V* relationship in response to hyperpolarizing current injections. Voltage sag was calculated as (peak-steady state)/peak for current injection of −500 pA or −250 pA for Etruscan shrew neurons owing to their very high input resistances. Spike full width at half maximum and area were computed using the base (calculated as the lowest voltage where the first derivative crossed 2 V s^{-1}) and the absolute peak of the spike. Previously published rat and human data analysed the same way were included in the larger datasets here[4]. Distal dendrites and proximal dendrites were 10–50% and 82–94% of somatic depth, respectively. The corresponding physical distances from the soma have the following ranges for distal (mouse 280–400 µm, gerbil 400–490 µm, rat 420–670 µm, guinea pig 580–909 µm, rabbit 734–1,000 µm, human 900–1,638 µm) and proximal (mouse 30–80 µm, gerbil 75–150 µm, rat 90–150 µm, guinea pig 125–150 µm, rabbit 107–190 µm, human 200–300 µm) dendrites. Reversal potentials were −30.7 mV for HCN[15], −69.9 mV for K_v peak and −85.5 for K_v plateau[24]. The end of the somatic compartment was defined as half the maximal width of the soma away from the maximal width of the soma. The end of the apical dendrite used for conductance estimation was 30% of the somatic depth. Cortical neuronal density (Extended Data Table 1) were converted to neurons per μm^3 for Fig. 4h using the brain-specific density (1.036 g cm^{-3}) (ref. [33]).

For nucleated patches, the central (biggest) cross-section was used to compute the major and minor axes from two-photon stacks (around 0.1 × 0.1 µm resolution; 0.5–1 µm steps). The surface area (*A*) was calculated as (π/4) × (major axis + minor axis). Morphological width measurements were performed after the patch pipette was removed. From two-photon stacks (1 µm steps) with variable zoom depending on the size of the region of interest, the central (brightest) cross-section was isolated. The image was rotated such that the soma and/or dendrite is vertical. Pixel intensity for segments of 2–10 µm were averaged and the full width at half maximum was computed as an estimate of the width. In calculating surface areas, the width was multiplied by the number of branches for dendrites post-branching points. *Z*-stack montage images were constructed using ImageJ on two-dimensional maximal intensity projections of 1–2 µm *z*-series collected at the end of the experiment.

Statistical analysis was performed in MATLAB. D'Agostino–Pearson tests were used to assess normality. For normal data, results are presented as mean ± s.e.m., and ANOVA or two-sided *t*-test were used for statistical analyses. For most skewed datasets, box plots denote the median and 25–75th percentiles, and two-sided Wilcoxon rank-sum test or Kruskal–Wallis test were used for statistical analysis. Median and 95% confidence intervals obtained with bootstrapping are presented for firing rates and interspike intervals as a function of injected current. No repeated measurements were used in this study. Statistical details can be found in the figure legends and in the main text. Reported *n* values can be found in the figure legends and in the results.

Reporting summary

Further information on research design is available in the Nature Research Reporting Summary linked to this paper.

Data availability

All data generated and supporting the findings of this study are presented in the paper. Additional information will be made available upon reasonable request.

18. Naumann, R. K., Anjum, F., Roth-Alpermann, C. & Brecht, M. Cytoarchitecture, areas, and neuron numbers of the Etruscan shrew cortex. *J. Comp. Neurol.* **520**, 2512–2530 (2012).
19. Paxinos G. & Watson C. *The Rat Brain in Stereotaxic Coordinates* 7th edn (Academic Press, 2013).
20. Hutchinson, E. B. et al. Population based MRI and DTI templates of the adult ferret brain and tools for voxelwise analysis. *Neuroimage* **152**, 575–589 (2017).
21. Muñoz-Moreno, E. et al. A magnetic resonance image based atlas of the rabbit brain for automatic parcellation. *PLoS ONE* **8**, e67418 (2013).
22. Yuasa, S., Nakamura, K. & Kohsaka, S. *Stereotaxic Atlas of the Marmoset Brain* (National Institute of Neuroscience (JP), 2010).
23. Paxinos, G., Petrides, M. & Evrard, H. *The Rhesus Monkey Brain in Stereotaxic Coordinates* 4th edn (Elsevier, 2021).
24. Bekkers, J. M. Properties of voltage-gated potassium currents in nucleated patches from large layer 5 cortical pyramidal neurons of the rat. *J. Physiol.* **525**, 593–609 (2000).
25. Ramaswamy, S. & Markram, H. Anatomy and physiology of the thick-tufted layer 5 pyramidal neuron. *Front. Cell. Neurosci.* **9**, 233 (2015).
26. Hay, E., Hill, S., Schurmann, F., Markram, H. & Segev, I. Models of neocortical layer 5b pyramidal cells capturing a wide range of dendritic and perisomatic active properties. *PLoS Comput. Biol.* **7**, e1002107 (2011).
27. Hodge, R. D. et al. Conserved cell types with divergent features in human versus mouse cortex. *Nature* **573**, 61–68 (2019).
28. Carnevale, N. T. & Hines, M. L. *The NEURON Book* (Cambridge University Press, 2006).
29. Larkum, M. E., Nevian, T., Sandler, M., Polsky, A. & Schiller, J. Synaptic integration in tuft dendrites of layer 5 pyramidal neurons: a new unifying principle. *Science* **325**, 756–760 (2009).
30. Miller, D. J., Balaram, P., Young, N. A. & Kaas, J. H. Three counting methods agree on cell and neuron number in chimpanzee primary visual cortex. *Front. Neuroanat.* **8**, 36 (2014).
31. Pilati, N., Barker, M., Panteleimonitis, S., Donga, R. & Hamann, M. A rapid method combining Golgi and Nissl staining to study neuronal morphology and cytoarchitecture. *J. Histochem. Cytochem.* **56**, 539–550 (2008).
32. Engel, D. & Jonas, P. Presynaptic action potential amplification by voltage-gated Na^+ channels in hippocampal mossy fiber boutons. *Neuron* **45**, 405–417 (2005).
33. Herculano-Houzel, S. *The Human Advantage: A New Understanding of How Our Brain Became Remarkable* (MIT Press, 2016).
34. Jardim-Messeder, D. et al. Dogs have the most neurons, though not the largest brain: trade-off between body mass and number of neurons in the cerebral cortex of large carnivoran species. *Front. Neuroanat.* **11**, 118 (2017).

Acknowledgements We thank M. Tadross, S. Herculano-Houzel, M. T. Do, A. Chang, C. Yaeger, V. Francioni and A. Landau for comments on the manuscript; M. Brecht for the gift of Etruscan shrews; J. Haupt for veterinary assistance with procedures; Z. Fu, G. Feng, R. Desimone, M. Jazayeri, E. Miller, M. De-Medonsa, M. Livingstone, M. Greenberg, G. Boulting, A. Chang, C. Walsh and E. DeGennaro for their help with tissue acquisition; J. Fox and the division of comparative medicine (DCM) at MIT for expert care and supervision of animals; B. Coughlin for help with the epileptic rats; and A. O'Donnell, A. Paulk and Y. Chou for assistance in acquiring human tissue. L.B.-L. was supported by the Natural Sciences and Engineering Research Council of Canada (NSERC) (PGSD2-517068-2018) and a Friends of the McGovern Institute fellowship. E.H.S.T. was supported by the National Institute of General Medical Sciences (T32GM007753) and the Paul & Daisy Soros Fellowship. M.T.H. was supported by the Dana Foundation David Mahoney Neuroimaging Grant Program, the NIH (RO1NS106031) and the Harvard–MIT Joint Research Grants Program in Basic Neuroscience. M.T.H. is a Klingenstein-Simons Fellow, a Vallee Foundation Scholar and a McKnight Scholar.

Author contributions L.B.-L. designed experiments, collected human brain samples, extracted animal brains, prepared slices, performed electrophysiological recordings, analysed data, prepared the figures and wrote the manuscript. N.J.B. performed and analysed electrophysiological recordings, prepared fixed tissues for histology, performed histological stainings and created illustrations for the figures. M.H. performed and analysed electrophysiological recordings. E.H.S.T. performed biophysical modelling. J.S. performed animal surgeries. Z.M.W. and G.R.C. performed the surgeries that resulted in the human tissue. M.P.F. oversaw the removal and parcellation of that tissue as well as overall IRB aspects and regulatory aspects of the project with regard to human participants. S.S.C. helped in designing methods for acquiring human tissue and ensured that the tissue was collected. M.T.H supervised all aspects of the project.

Competing interests The authors declare no competing interests.

Additional information
Supplementary information The online version contains supplementary material available at https://doi.org/10.1038/s41586-021-04072-3.

Correspondence and requests for materials should be addressed to Mark T. Harnett.

Peer review information *Nature* thanks the anonymous reviewers for their contribution to the peer review of this work.

Reprints and permissions information is available at http://www.nature.com/reprints.

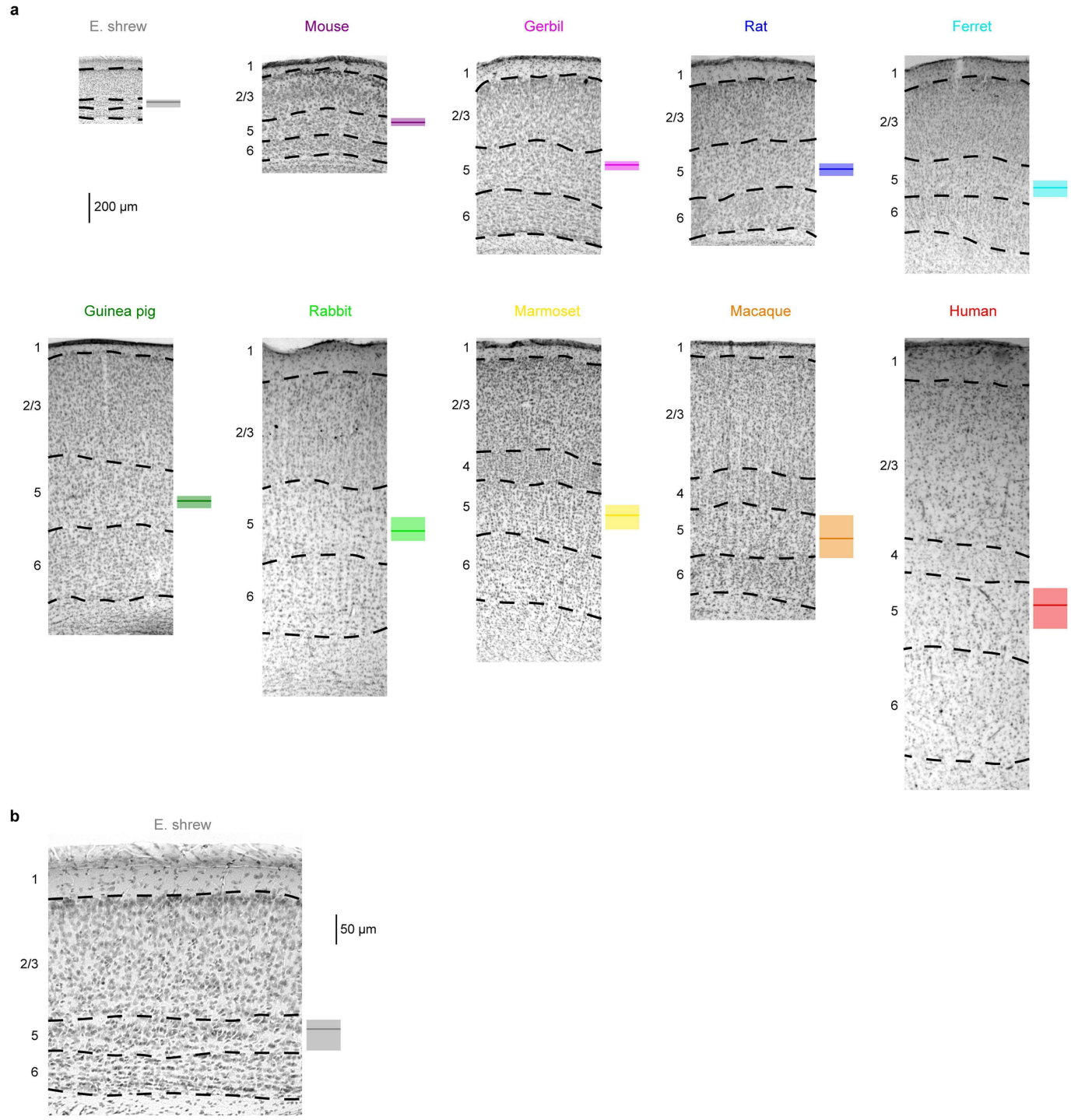

Extended Data Fig. 1 | Histological identification of cortical layers. Related to Fig. 1. a, Nissl-stained brain slices from the 10 species with labelled cortical layers. Box plots on the right of individual slices denote the median and 25–75th percentiles of somatic depth for electrophysiological recordings (Etruscan shrew n = 39, mouse n = 162, gerbil n = 105, rat n = 215, ferret n = 31, guinea pig n = 118, rabbit n = 87, marmoset n = 41, macaque n = 34, human n = 208). **b**, The shrew slice from a, expanded to show detail (n = 39).

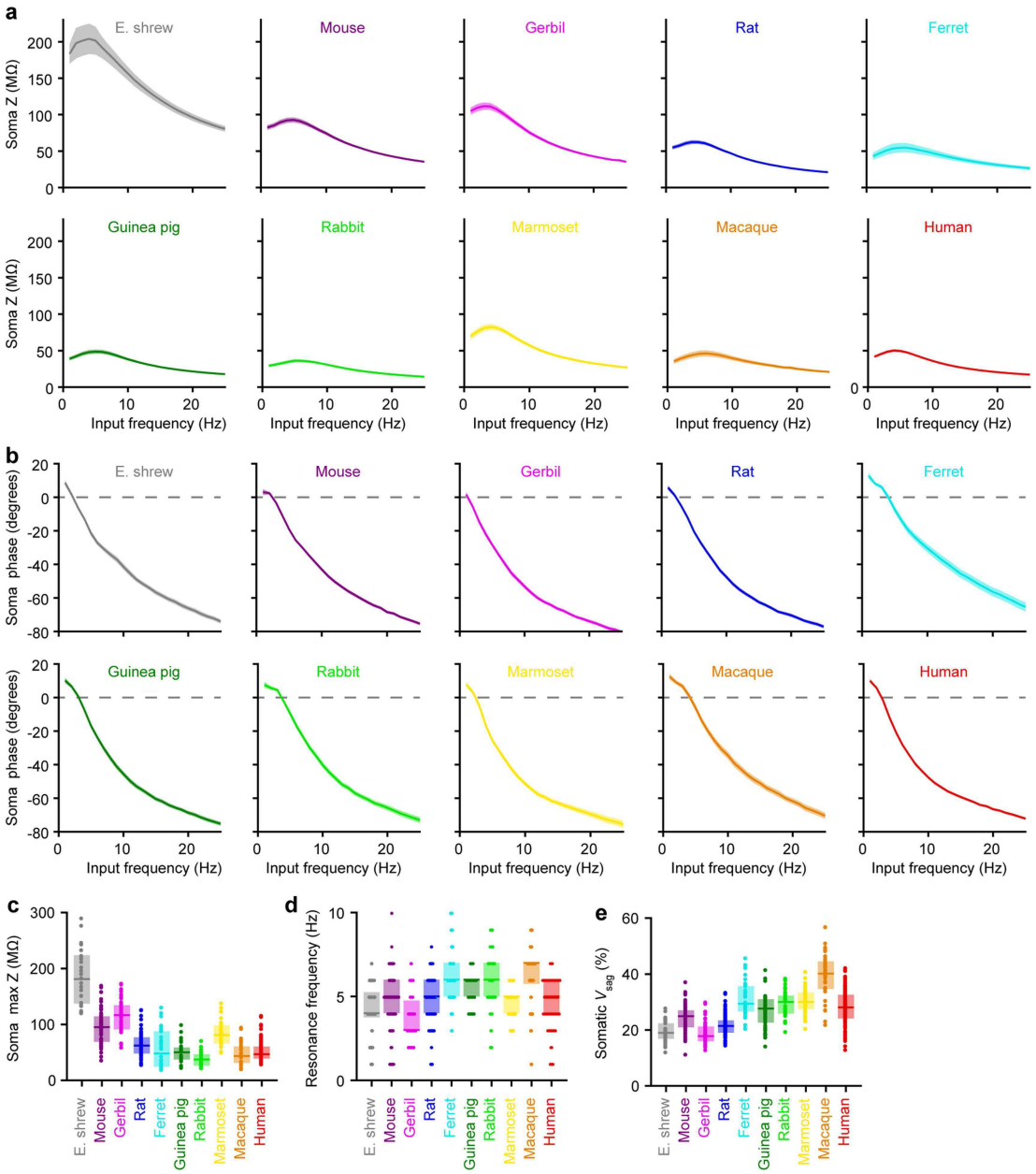

Extended Data Fig. 2 | Somatic impedance profiles and voltage sag. Related to Fig. 1. a-d, Somatic impedance profiles (Etruscan shrew n = 29, mouse n = 71, gerbil n = 39, rat n = 64, ferret n = 28, guinea pig n = 35, rabbit n = 37, marmoset n = 30, macaque n = 25, human n = 100). Pooled data represent mean ± SEM for a-b. Box plots denote the median and 25–75th percentiles for c-d. **a**, Impedance profile in response to sinewaves of 50-100 pA injected at the indicated frequencies for 2 s. **b**, Phase offset between the voltage response and the injected current. **c**, Maximal impedance ($p < 10^{-49}$ Kruskal-Wallis; $\chi^2 = 259$ & 9 df). **d**, Resonance frequency ($p < 10^{-13}$ Kruskal-Wallis; $\chi^2 = 81$ & 9 df). Data points displayed as a beeswarm plot to show overlapping integers. **e**, Somatic voltage sag ($p < 10^{-57}$ Kruskal-Wallis, $\chi^2 = 298$ & 9 df; Etruscan shrew n = 39, mouse n = 85, gerbil n = 58, rat n = 117, ferret n = 31, guinea pig n = 47, rabbit n = 40, marmoset n = 41, macaque n = 34, human n = 126). Box plots denote the median and 25–75th percentiles.

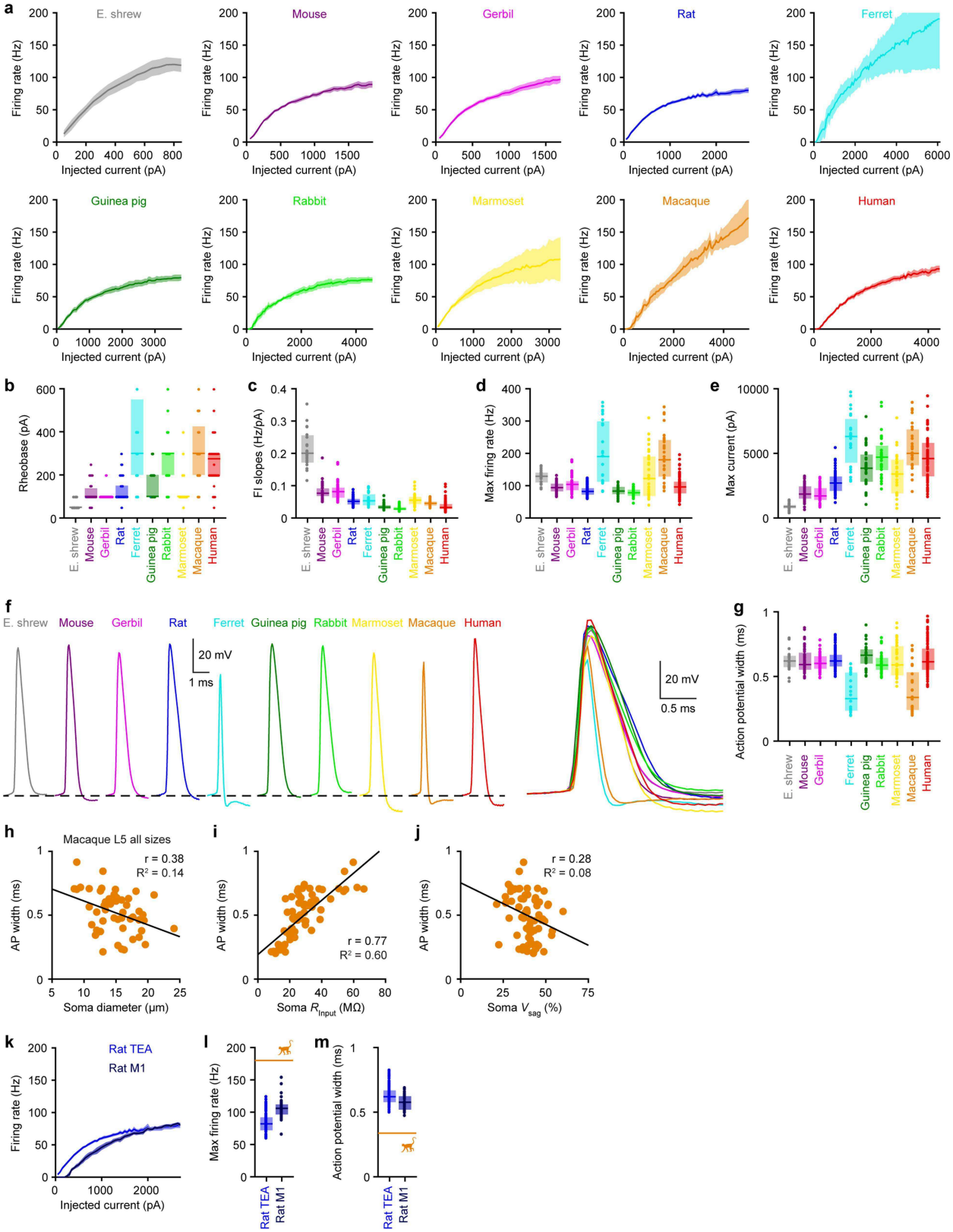

Extended Data Fig. 3 | See next page for caption.

Extended Data Fig. 3 | Somatic firing properties. Related to Fig. 1. Somatic firing properties (Etruscan shrew n = 22, mouse n = 59, gerbil n = 46, rat n = 93, ferret n = 23, guinea pig n = 30, rabbit n = 33, marmoset n = 34, macaque n = 29, human n = 104). **a**, Firing rates as a function of injected current. The lines and shaded error bars represent population medians and 95% confidence intervals. **b**-**g**, Box plots denote the median and 25–75th percentiles. **b**, Rheobase ($p < 10^{-47}$ Kruskal-Wallis, $\chi^2 = 250$ & 9 df). Data points displayed as a beeswarm plot to show overlapping integers. **c**, Slope of firing rate-current relationship ($p < 10^{-59}$ Kruskal-Wallis, $\chi^2 = 304$ & 9 df). **d**, Maximal firing rate ($p < 10^{-26}$ Kruskal-Wallis, $\chi^2 = 146$ & 9 df). **e**, Maximal current eliciting action potentials before entering depolarization block ($p < 10^{-54}$ Kruskal-Wallis, $\chi^2 = 283$ & 9 df). **f**, Representative action potential waveforms. **g**, Width of first action potential at rheobase ($p < 10^{-13}$ Kruskal-Wallis, $\chi^2 = 86$ & 9 df). **h**-**j**, Correlation between action potential width (at rheobase) and other parameters for macaque L5 neurons of different somatic sizes (not restricted to large L5 with thick dendrites). **h**, Correlation with soma diameter ($R^2 = 0.145$, $p = 0.006$, linear regression, $F = 8.3$ & 49 df, n = 51). **i**, Correlation with soma input resistance ($R^2 = 0.596$, $p < 10^{-13}$, linear regression, $F = 94.5$ & 64 df, n = 66). **j**, Correlation with soma voltage sag (n = 66; $R^2 = 0.079$, $p = 0.02$, linear regression, $F = 5.5$ & 64 df, n = 66). **k**-**m**, Rat somatic firing properties of L5b neurons in TEA (n = 93) versus M1 (n = 39). Orange lines represent median L5 macaque data from Extended Data Fig. 3d, g. **k**, Firing rates as a function of injected current. The lines and shaded error bars represent population medians and 95% confidence intervals. **l**, Maximal firing rate ($p < 10^{-8}$, two-sided Wilcoxon rank sum, $Z = -5.93$). **m**, Width of first action potential at rheobase ($p < 10^{-3}$, two-sided Wilcoxon rank sum, $Z = 3.34$).

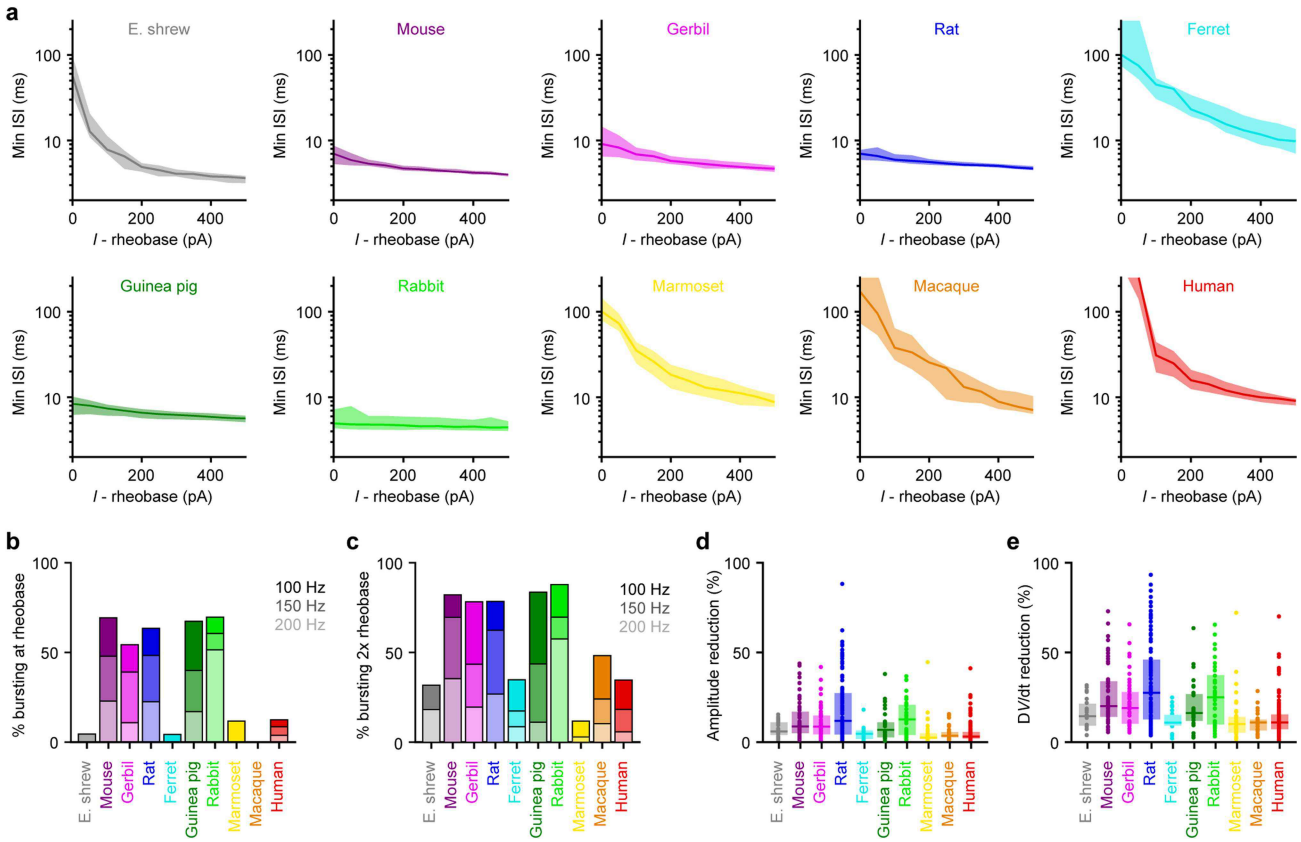

Extended Data Fig. 4 | Somatic bursting properties. Related to Fig. 1. Somatic bursting properties (Etruscan shrew n = 22, mouse n = 59, gerbil n = = 46, rat n = 93, ferret n = 23, guinea pig n = 30, rabbit n = 33, marmoset n = 34, macaque n = 29, human n = 104). **a**, Minimum instantaneous interspike interval (ISI) on a log scale as a function of injected current above rheobase. The lines and shaded error bars represent population medians and 95% confidence intervals. **b**, Percentage of neurons exhibiting bursts with different frequency thresholds at rheobase. **c**, Same as b but at double the rheobase. **d**-**e**, Box plots denote the median and 25–75th percentiles. **d**, Maximal action potential amplitude reduction ($p < 10^{-18}$ Kruskal-Wallis, $\chi^2 = 107$ & 9 df). **e**, Maximal action potential d*V*/dt reduction ($p < 10^{-15}$ Kruskal-Wallis, $\chi^2 = 95$ & 9 df).

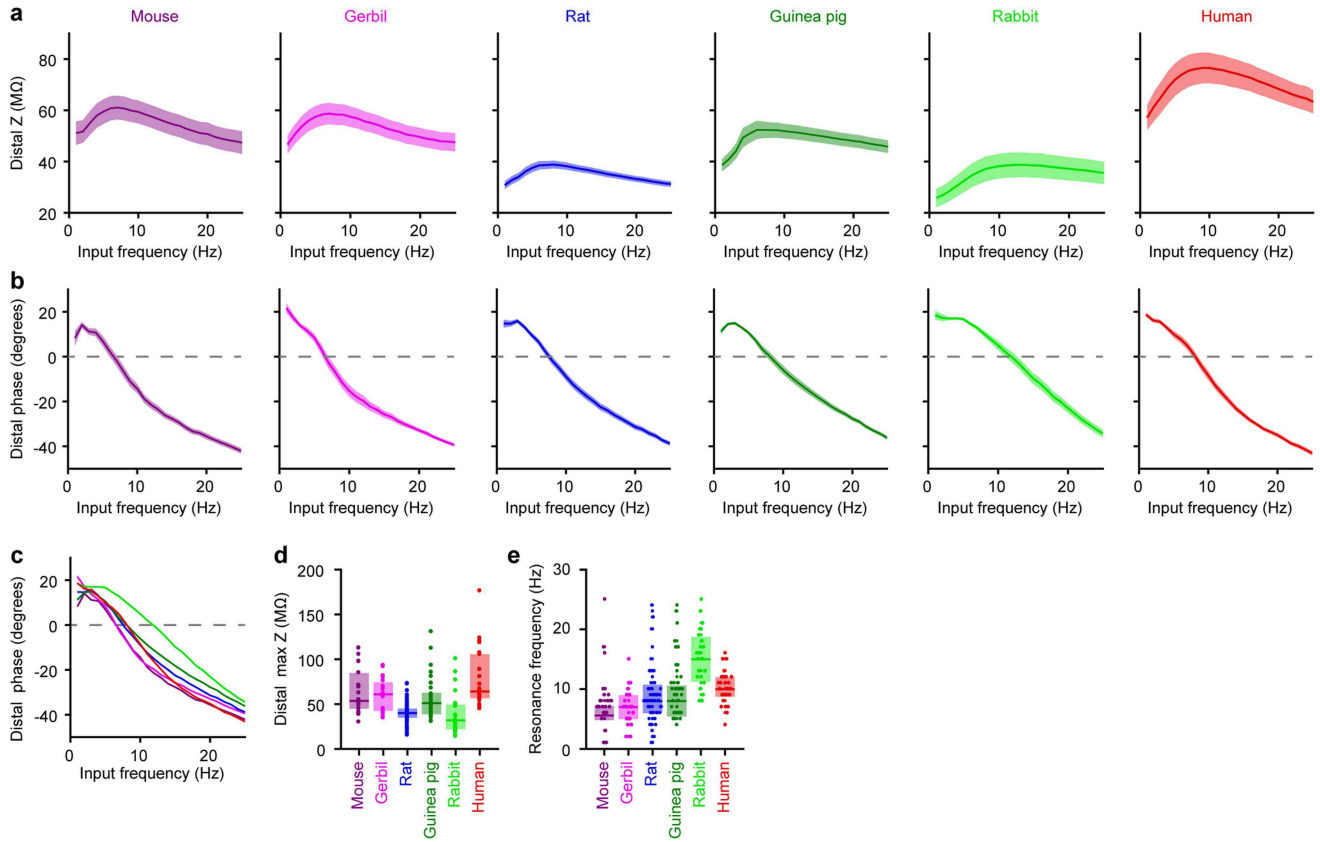

Extended Data Fig. 5 | Dendritic impedance profiles. Related to Fig. 2. Dendritic impedance profiles (mouse n = 26, gerbil n = 19, rat n = 59, guinea pig n = 37, rabbit n = 23, human n = 25). Pooled data represent mean ± SEM for a-b. Box plots denote the median and 25–75th percentiles for d-e. **a**, Impedance profile in response to sinewaves of 50-100 pA injected at the indicated frequencies for 2 s. **b**, Phase offset between the voltage response and the injected current. **c**, Mean data from b. **d**, Maximal impedance ($p < 10^{-10}$ Kruskal-Wallis, $\chi^2 = 59$ & 5 df). **e**, Resonance frequency ($p < 10^{-6}$ Kruskal-Wallis, $\chi^2 = 39$ & 5 df). Data points displayed as a beeswarm plot to show overlapping integers.

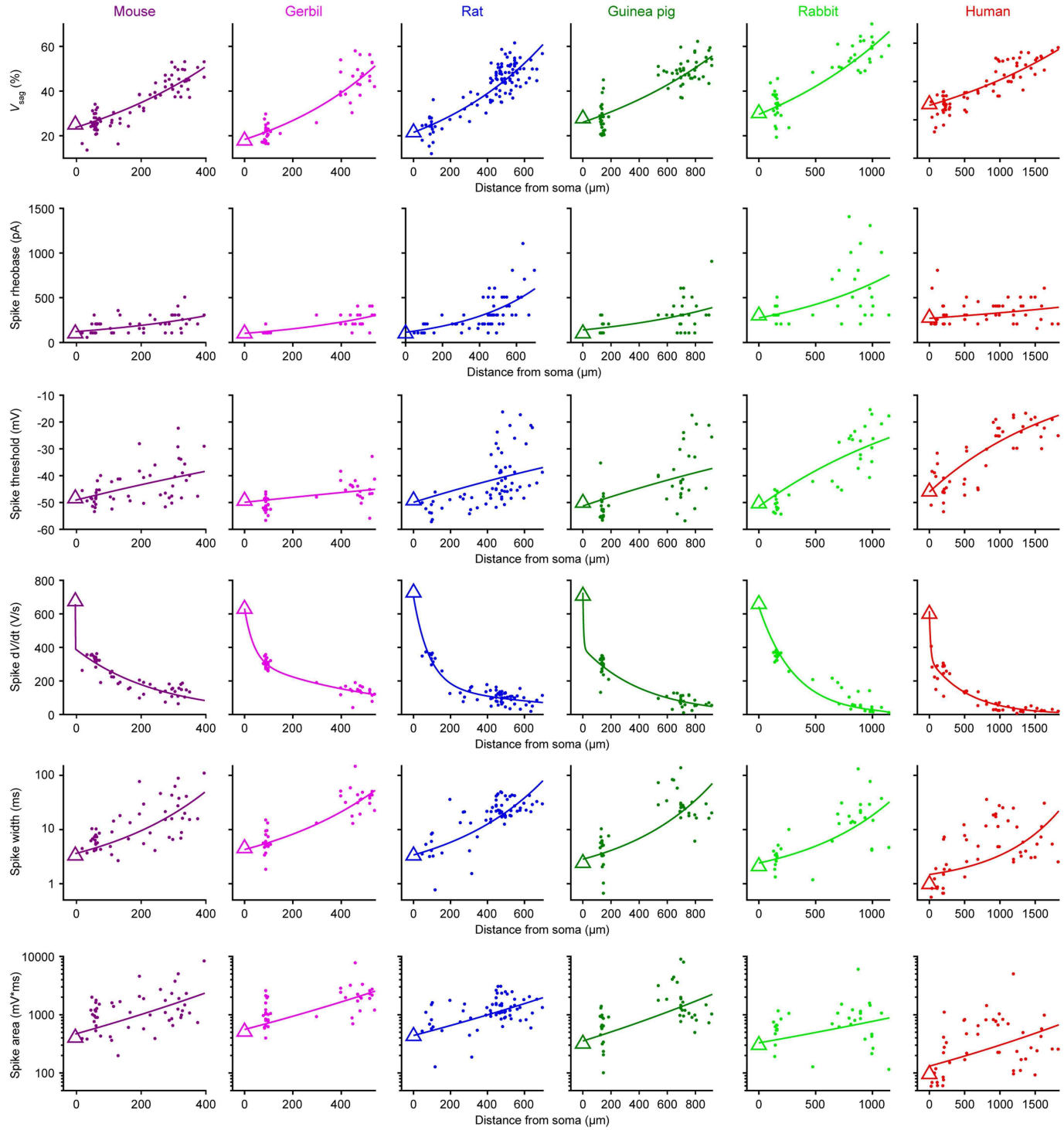

Extended Data Fig. 6 | Additional dendritic properties. Related to Fig. 2. Voltage sag (mouse n = 76, gerbil n = 47, rat n = 108, guinea pig n = 71, rabbit n = 47, human n = 72), resting membrane potential (mouse n = 76, gerbil n = 47, rat n = 108, guinea pig n = 71, rabbit n = 47, human n = 72), and spike properties (mouse n = 51, gerbil n = 40, rat n = 65, guinea pig n = 45, rabbit n = 35, human n = 49) as a function of distance from the soma. Triangles are somatic medians. Lines are an exponential fit to the data or double exponential fit for spike d*V*/dt. Spike width and area are on a log scale.

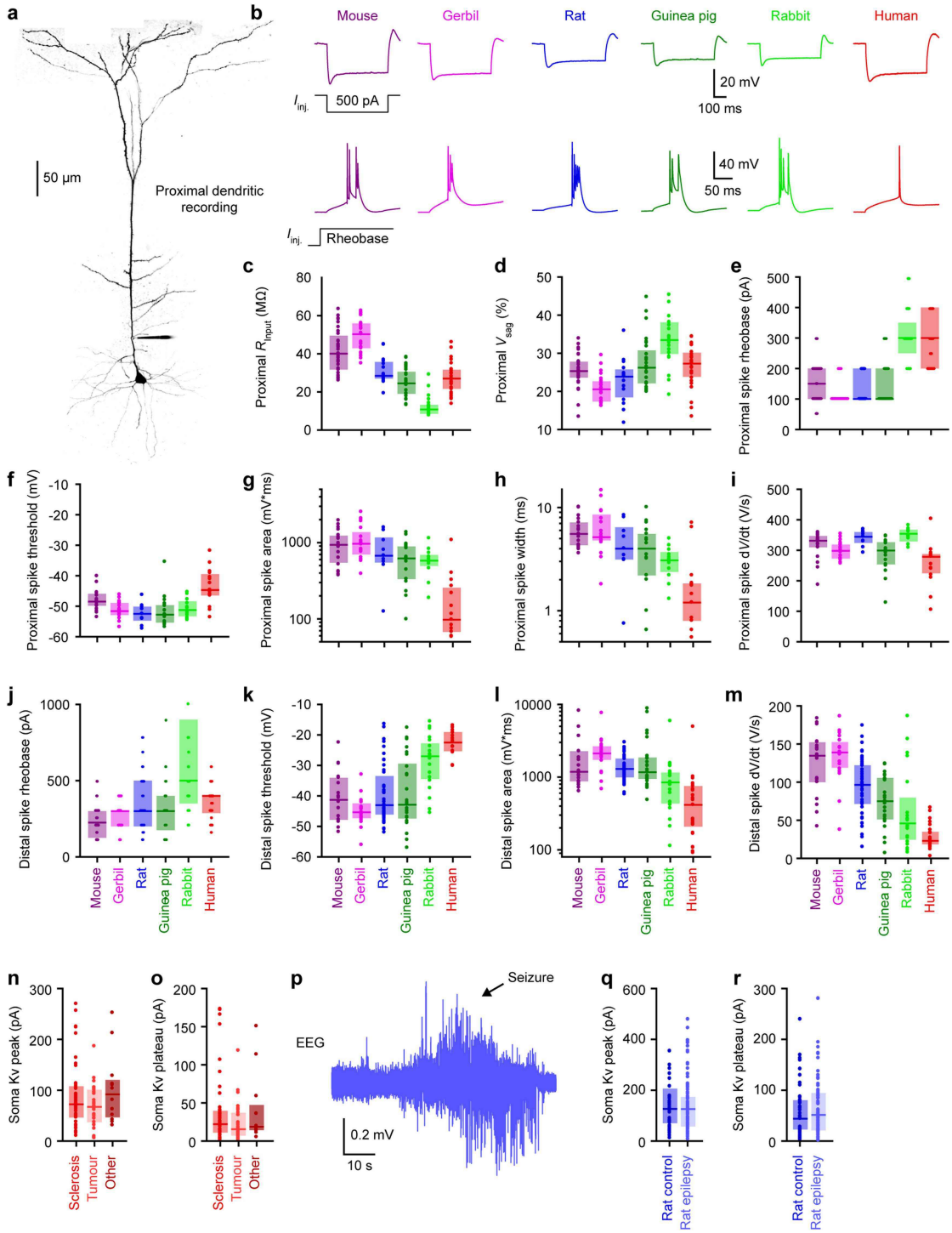

Extended Data Fig. 7 | See next page for caption.

Extended Data Fig. 7 | Proximal dendritic properties and additional distal dendritic properties. Related to Fig. 2. **a**, Two-photon *z*-stack montage image of mouse neuron with a proximal patch-clamp electrode 63 µm from soma. **b**, Proximal dendritic voltage in response to subthreshold (top) or threshold (bottom) step current injections. **c**-**d**, Subthreshold properties of proximal dendrites (mouse n = 31, gerbil n = 23, rat n = 19, guinea pig n = 28, rabbit n = 21, human n = 27). Box plots denote the median and 25–75th percentiles. **c**, Proximal input resistance ($p < 10^{-18}$ Kruskal-Wallis, $\chi^2 = 98$ & 5 df). **d**, Proximal voltage sag ($p < 10^{-8}$ Kruskal-Wallis, $\chi^2 = 47$ & 5 df). **e**-**i**, Suprathreshold properties of proximal dendrites (mouse n = 19, gerbil n = 20, rat n = 9, guinea pig n = 18, rabbit n = 12, human n = 15). Box plots denote the median and 25–75th percentiles. **e**, Proximal rheobase ($p < 10^{-9}$ Kruskal-Wallis, $\chi^2 = 51$ & 5 df). Data points displayed as a beeswarm plot to show overlapping integers. **f**, Proximal spike threshold ($p < 10^{-4}$ Kruskal-Wallis, $\chi^2 = 31$ & 5 df). **g**, Proximal spike area on a log scale ($p < 10^{-6}$ Kruskal-Wallis, $\chi^2 = 36$ & 5 df). **h**, Proximal spike width on a log scale ($p < 10^{-5}$ Kruskal-Wallis, $\chi^2 = 36$ & 5 df). **i**, Proximal maximum spike d*V*/dt ($p < 10^{-5}$ Kruskal-Wallis, $\chi^2 = 35$ & 5 df). **j**-**m**, Additional suprathreshold properties of distal dendrites (mouse n = 18, gerbil n = 19, rat n = 47, guinea pig n = 25, rabbit n = 20, human n = 25). Box plots denote the median and 25–75th percentiles. **j**, Distal rheobase ($p < 10^{-4}$ Kruskal-Wallis, $\chi^2 = 28$ & 5 df). Data points displayed as a beeswarm plot to show overlapping integers. **k**, Distal spike threshold ($p < 10^{-11}$ Kruskal-Wallis, $\chi^2 = 61$ & 5 df). **l**, Distal spike area on a log scale ($p < 10^{-10}$ Kruskal-Wallis, $\chi^2 = 58$ & 5 df). **m**, Maximum distal spike d*V*/dt ($p < 10^{-13}$ Kruskal-Wallis, $\chi^2 = 74$ & 5 df). **n**-**o**, Somatic outside-out currents in sclerosis (n = 44), tumour (n = 30) and others (n = 12). Box plots denote the median and 25–75th percentiles. **n**, Somatic K_v peak currents (p = 0.39 Kruskal-Wallis, $\chi^2 = 1.90$ & 2 df). **o**, Somatic K_v plateau currents (p = 0.35 Kruskal-Wallis, $\chi^2 = 2.09$ & 2 df). **p**, Example EEG recording of epileptic seizure in rat kainic acid model. **q**-**r**, Somatic outside-out currents in control (n = 80) and epileptic (n = 68) rats. Box plots denote the median and 25–75th percentiles. **q**, Somatic K_v peak currents (p = 0.65, two-sided Wilcoxon rank sum, Z = 0.45). **r**, Somatic K_v plateau currents (p = 0.525, two-sided Wilcoxon rank sum, Z = 0.64).

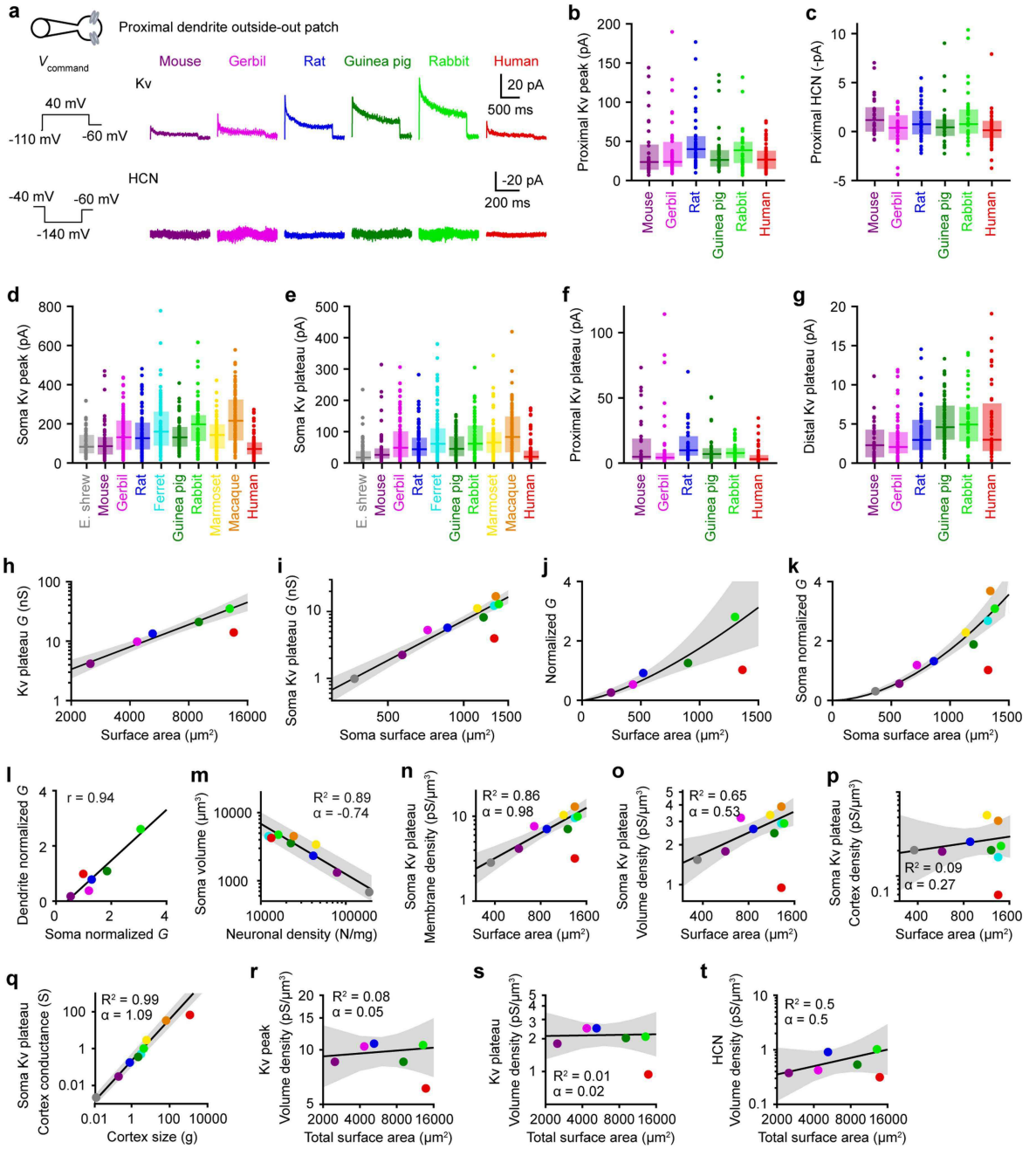

Extended Data Fig. 8 | See next page for caption.

Extended Data Fig. 8 | Additional conductance measurements. Related to Fig. 3. a, Dendritic outside-out patches were pulled from proximal dendrites after obtaining whole-cell recordings. Top, HCN currents with the associated voltage-clamp protocol on the left. Bottom, K_v currents with the associated voltage-clamp protocol on the left. **b**-**g**, Box plots denote the median and 25–75th percentiles. **b**, Proximal K_v peak currents ($p = 0.010$ Kruskal-Wallis, $\chi^2 = 15$ & 5 df; mouse n = 32, gerbil n = 38, rat n = 38, guinea pig n = 37, rabbit n = 35, human n = 44). **c**, Proximal HCN steady-state currents ($p=0.07$ Kruskal-Wallis, $\chi^2 = 10$ & 5 df; mouse n = 29, gerbil n = 30, rat n = 38, guinea pig n = 30, rabbit n = 31, human n = 42). **d**, Somatic K_v peak currents ($p < 10^{-19}$ Kruskal-Wallis, $\chi^2 = 115$ & 9 df; Etruscan shrew n = 59, mouse n = 56, gerbil n = 80, rat n = 80, ferret n = 80, guinea pig n = 70, rabbit n = 53, marmoset n = 63, macaque n = 87, human n = 86). **e**, Somatic K_v plateau currents ($p < 10^{-19}$ Kruskal-Wallis, $\chi^2 = 115$ & 9 df; Etruscan shrew n = 59, mouse n = 56, gerbil n = 80, rat n = 80, ferret n = 80, guinea pig n = 70, rabbit n = 53, marmoset n = 63, macaque n = 87, human n = 86). **f**, Proximal K_v plateau currents ($p < 10^{-4}$ Kruskal-Wallis, $\chi^2 = 29$ & 5 df; mouse n = 32, gerbil n = 38, rat n = 38, guinea pig n = 26, rabbit n = 35, human n = 44). **g**, Distal K_v plateau currents ($p = 0.00001$ Kruskal-Wallis, $\chi^2 = 30$ & 5 df; mouse n = 35, gerbil. n = 46, rat n = 59, guinea pig n = 58, rabbit n = 39, human n = 43). **h**-**k**, Conductance as a function of neuron size. The lines and shaded error bars represent the fit and 95% confidence interval of an allometric relationship constructed excluding humans. **h**, Total K_v plateau conductance on a log-log scale (exponent 1.24 ± 0.09, $R^2 = 0.983$, $p < 10^{-3}$, linear regression on log-log scale, $F = 176$ & 3 df, n = 5 for mouse, gerbil, rat, guinea pig, and rabbit). **i**, Somatic K_v plateau conductance on a log-log scale (exponent 1.98 ± 0.15, $R^2 = 0.962$, $p < 10^{-5}$, linear regression on log-log scale, $F = 175$ & 7 df, n = 9 for shrew, mouse, gerbil, rat, ferret, guinea pig, rabbit, marmoset, and macaque). **j**, Normalized average of HCN, K_v peak and K_v plateau conductance (exponent 1.43 ± 0.15, $R^2 = 0.966$, $p = 0.003$, linear regression on log-log scale, $F = 85.7$ & 3 df, n = 5 for mouse, gerbil, rat, guinea pig, and rabbit). **k**, Normalized average of somatic K_v peak and K_v plateau conductance (exponent 1.82 ± 0.12, $R^2 = 0.968$, $p < 10^{-5}$, linear regression on log-log scale, $F = 212$ & 7 df, n = 9 for shrew, mouse, gerbil, rat, ferret, guinea pig, rabbit, marmoset and macaque). **l**, Relationship between somatic (normalized average of somatic K_v peak and K_v plateau conductance) and dendritic (normalized average of HCN, K_v peak and K_v plateau conductance) conductance ($R^2 = 0.891$, $p = 0.005$, linear regression, $F = 32.7$ & 4 df, n = 6 for mouse, gerbil, rat, guinea pig, rabbit, and human). **m**, Soma volume as a function of neuronal density (Extended Data Table 1) on a log-log scale (exponent -0.74 ± 0.10, $R^2 = 0.897$, $p < 10^{-3}$, linear regression, $F = 52.3$ & 6 df, n = 8 for shrew, mouse, rat, ferret, guinea pig, rabbit, marmoset, and macaque). The line and shaded error bars represent the fit and 95% confidence interval of an allometric relationship constructed excluding humans. **n**-**t**, Allometric relationship on a log-log scale. The lines and shaded error bars represent the fit and 95% confidence interval of the relationship constructed excluding humans. **n**-**o**, Somatic K_v plateau conductance densities in volumes as in Fig. 4c. **n**, Membrane conductance density (exponent 0.98 ± 0.15, $R^2 = 0.860$, $p < 10^{-3}$, linear regression, $F = 43.0$ & 7 df, n = 9 for shrew, mouse, gerbil, rat, ferret, guinea pig, rabbit, marmoset, and macaque). **o**, Volume K_v peak conductance density where the volume is filled with somas (exponent 0.53 ± 0.15, $R^2 = 0.651$, $p = 0.009$, linear regression, $F = 13.1$ & 7 df, n = 9 for shrew, mouse, gerbil, rat, ferret, guinea pig, rabbit, marmoset, and macaque). **p**-**q**, Somatic K_v plateau conductance densities in volumes as in Fig. 4g. Gerbils were not included because the necessary information was not available in the literature (Extended Data Table 1). **p**, Cortex conductance density with accurate neuronal densities (exponent -0.27 ± 0.34, $R^2 = 0.092$, $p = 0.47$, linear regression, $F = 0.61$ & 6 df, n = 8 for shrew, mouse, rat, ferret, guinea pig, rabbit, marmoset, and macaque). **q**, Total cortex conductance (exponent 1.09 ± 0.06, $R^2 = 0.985$, $p < 10^{-5}$, linear regression, $F = 393$ & 6 df, n = 8 for shrew, mouse, rat, ferret, guinea pig, rabbit, marmoset and macaque). **r**-**t**, Same analysis as in Fig. 4f, but including dendrites in the volume and conductance calculation. **r**, Volume K_v peak conductance density where the volume is filled with somas and dendrites (exponent 0.05 ± 0.10, $R^2 = 0.083$, $p = 0.64$, linear regression, $F = 0.272$ & 3 df, n = 5 for mouse, gerbil, rat, guinea pig, and rabbit). **s**, Volume K_v plateau conductance density where the volume is filled with somas and dendrites (exponent 0.02 ± 0.13, $R^2 = 0.006$, $p = 0.90$, linear regression, $F = 0.02$ & 3 df, n = 5 for mouse, gerbil, rat, guinea pig, and rabbit). **t**, Volume HCN conductance density where the volume is filled with somas and dendrites (exponent 0.5 ± 0.29, $R^2 = 0.500$, $p = 0.18$, linear regression, $F = 2.99$ & 3 df, n = 5 for mouse, gerbil, rat, guinea pig, and rabbit).

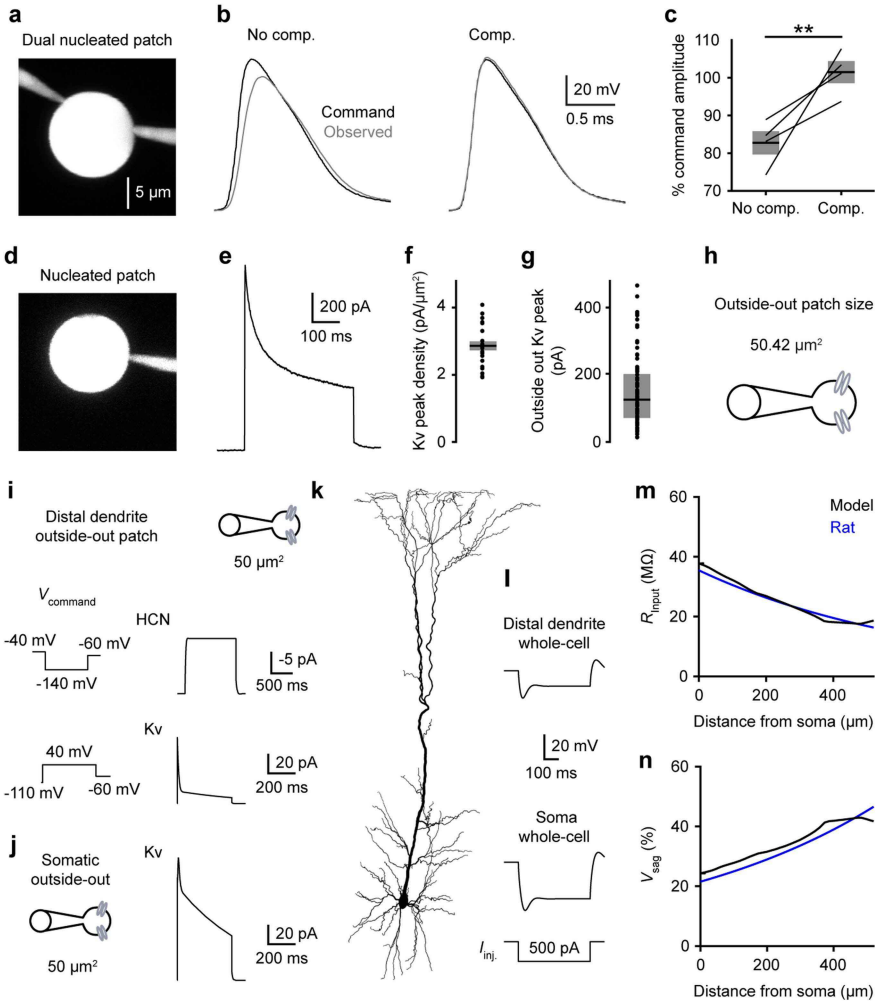

Extended Data Fig. 9 | Outside-out patch size estimation. Related to Fig. 3. **a**, Rat dual nucleated patch recordings to test the efficacy of voltage-clamp under nucleated patch configuration. **b**, Voltage-clamp command action potential waveform (black) and independently observed waveform (grey) without compensation (left) or with series resistance and whole-cell capacitance predicted and compensated >90% and lag <10 µs (right). **c**, Percentage of command waveform amplitude observed with the independent electrode (n = 4; p = 0.0045, two-sided paired t test, t = 4.41 & 6 df). Pooled data represent mean ± SEM. **d**, Rat nucleated patch recording with series resistance and whole-cell capacitance predicted and compensated >90% and lag <10 µs. **e**, K_v currents from the recording in d. **f**, Rat K_v peak current density computed using the K_v currents and patch surface area (n = 22). Pooled data represent mean ± SEM. **g**, Rat K_v peak currents in somatic outside-out patch (n = 80). Box plots denote the median and 25–75th percentiles. **h**, Outside-out patch surface area computed using the mean K_v peak current density in f and the median K_v peak current in g. **i-j**, Recapitulation of outside-out patch recordings in a compartmental model of rat L5 neuron. **i**, Model dendritic outside-out patches as spheres of 50 µm². HCN (top) and K_v (bottom) currents (right) with associated voltage-clamp protocol (left). **j**, Model K_v currents in somatic outside-out patches. **k**, Morphology used in the model taken from (https://senselab.med.yale.edu/ModelDB/ShowModel?model=124043#tabs-3). **l**, Distal dendritic (520 µm from soma) and somatic voltage in response to subthreshold step current injections in the model. **m**, Somatic and dendritic input resistance as a function of distance from the soma. Fit to experimental rat data in blue taken from Fig. 2d versus model data in black. **n**, Somatic and dendritic voltage sag as a function of distance from the soma. Fit to experimental rat data in blue taken from Extended Data Fig. 6 versus model data in black.

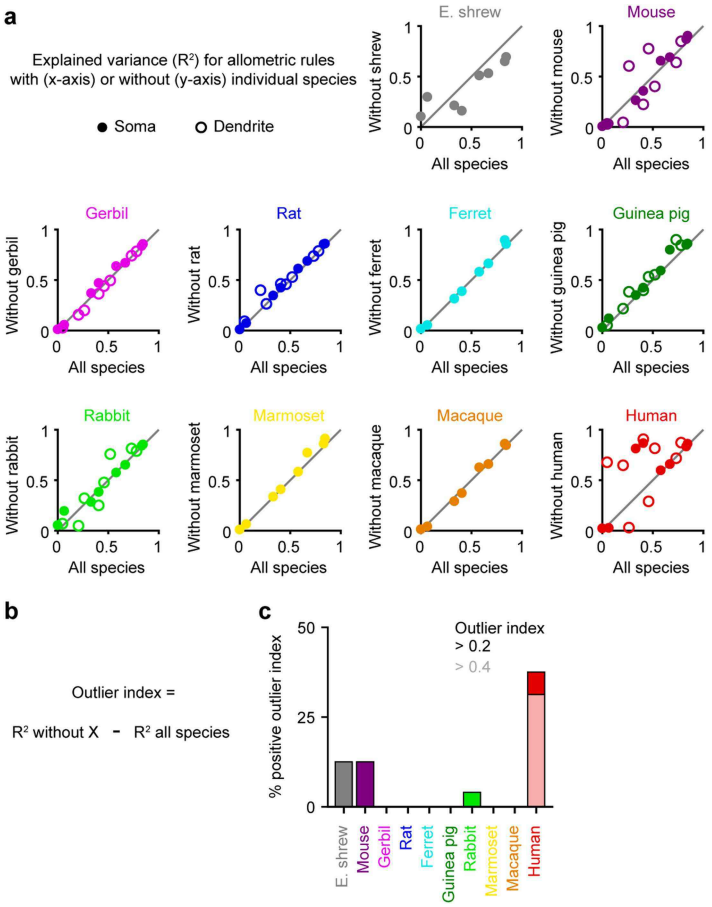

Extended Data Fig. 10 | Only human neurons are consistent outliers in electrophysiological features. Related to Fig. 4. a, Explained variance of allometric relationship with (x-axis) versus without (y-axis) individual species for the same electrophysiological properties as in Fig. 4b. **b**, Calculation of outlier index. Positive outlier indices reflect cases in which a given species is an outlier and does not follow a conserved pattern observed in the other species. **c**, Percentage of features with substantial positive outlier indices (threshold at 0.2 or 0.4) for the different species.

Extended Data Table 1 | Species information

Species	Cortex size (g)	Cortical neurons (N)	Cortical neuronal density (N/mg)
Etruscan shrew	0.01098	2,100,000	191,229
Mouse	0.173	13,688,162	78,672
Gerbil	N/A	N/A	N/A
Rat	0.769	31,017,192	41,092
Ferret	3.123	38,950,000	12,473
Guinea pig	1.938	43,510,525	22,508
Rabbit	4.448	71,488,750	16,063
Marmoset	5.561	244,720,000	44,280
Macaque	69.832	1,710,000,000	24,470
Human	1,232.93	16,340,000,000	13,520

Mouse, rat, guinea pig, rabbit, marmoset, macaque and human data points were taken directly from Table 1 in a previous study[10]. Gerbil data were not available. Ferret data were taken from Table 1 in a previous study[34]. For Etruscan shrews, the cortical volume was found to be 5.3 ± 1.4 mm^3 per hemisphere[18]. The volume was doubled for total cortical volume and converted to mass (0.01098 g) using the brain specific density (1.036 g cm^{-3}) (ref. [33]). Using cortex size and number of cortical neurons[3], we calculated neuronal density (191,229 N mg^{-1}).

Extended Data Table 2 | Breakdown of dataset of 2,257 recordings from temporal cortex

	Whole cell		Outside-out	
	Soma	Dendrite	Soma	Dendrite
Etruscan shrew	39	-	59	-
Mouse	85	76	56	67
Gerbil	58	47	80	84
Rat	117 (82)	108 (89)	80	97 (56)
Ferret	31	-	80	-
Guinea pig	47	71	70	95
Rabbit	40	47	53	74
Marmoset	41	-	63	-
Macaque	34	-	87	-
Human	126 (39)	72 (42)	86	87 (34)
Total	**618 (121)**	**421 (131)**	**714**	**504 (90)**

Number of whole-cell and outside-out recordings per species. A total of 342 recordings came from our previously published dataset[4] and are shown in the parentheses. There are an additional 170 recordings not included in the 2,257 count that come from epileptic rats (Extended Data Fig. 7p-r), rat M1 (Extended Data Fig. 3k-m), nucleated patches (Extended Data Fig. 9) and macaque recordings from L5 of all sizes (Extended Data Fig. 3h-j).

Extended Data Table 3 | Information on patients with epilepsy (related to Methods)

Sex	Age	Hande-dness	Age at epilepsy onset	Pathological observations	Seizure frequency	Antiepileptic drugs (pre-surgery)	Brain region
Sclerosis cases							
M	26	R	21	Hippocampal Sclerosis and low-grade neuronal lesion	0.5 – 1 / month	LEV, LTG, CBZ	R ATL
M	37	R	1	Hippocampal Sclerosis	1-2 / month	LTG, LEV, LCM	L ATL
M	32	R	29	Hippocampal Sclerosis	Daily	LCM, LTG	L ATL
M	28	R	13	Hippocampal Sclerosis	15 / month; at least weekly	LEV, BZD2, OXC	R ATL
M	28	R	2	Hippocampal Sclerosis	2-3 / month	CLB, LTG	L ATL
F	40	R	21	Hippocampal Sclerosis	4-5 / month	LEV, LTG, BZD2	R ATL
F	42	R	15	Hippocampal Sclerosis	3-4 / month	LEV, LTG	R ATL
F	22	R	16	Hippocampal Sclerosis	~12 / month	OXC	R ATL
M	27	R	23	Hippocampal Sclerosis	4 / month	VPA, CBZ, CLB	R ATL
M	34	R	31	Hippocampal Sclerosis	0-5 / month	LCS, LEV	R ATL
F	55	R	48	Likely Mesial temporal sclerosis based on imaging / pathology = inconclusive	2-5 / month	CLB, LTG, LEV	L ATL
M	26	R	22	Hippocampal Sclerosis	3-7 / month	LTG, OXC	L ATL
M	22	L	7	Hippocampal Sclerosis	1 / month	LCM	L ATL (modified hemispherectomy)
M	57	R	11	Hippocampal Sclerosis	2-6 / year	BRV, LTG, ZNS	R ATL
F	48	R	14	Hippocampal Sclerosis	1 every 3-4 weeks	LTG, CLB	L ATL
Tumour cases							
F	26	R	19	Low grade glial/neuroglial tumour	1-2 / month	LTG, LEV	R ATL
F	50	R	46	Prior meningioma / pathology = normal	3-8 / month	ESL, LCS, LEV	R ATL
F	52	R	47	Dysembryoplastic neuroepithelial tumour (DNT), grade 1	20 /year	CBZ, LEV	L ATL
Other cases							
M	20	L	17	Moderate gliosis of the end folium (CA4) and the pyramidal cell layer (CA1)	12 / month	LEV, VPA, BZD1	L ATL
F	28	R	2	Focal Cortical Dysplasia Type IIIB (different location than resected tissue)	1-4 / month	LEV, LCS, ZNS,	R ATL
F	36	L	14	Post traumatic changes and hippocampal sclerosis	3-8 / month	LTG, ZNS, CLB	L ATL
M	58	R	30	Prior trauma / pathology = focal white matter hypercellularity and focal satellitosis in gray matter	Status 1-2 yearly, aura more frequently	LTG, LCS, LEV	R ATL and orbitofrontal. Recordings only in R ATL
M	48	L	18	Prior trauma but normal pathology	14 / month	VPA, ESL	R ATL
M	64	R	46	Chronic infarct	1 every 1-4 month	VPA, LEV, LCS	R ATL
M	23	L	17	Mild gliosis	~6 /year	LEV, LTG, LCS	L ATL
M	52	R	47	Prior trauma with gliosis and organized hematoma	1 every 1-2 month	LEV, ZNS, PHT	R ATL

Male (M), female (F), left (L), right (R), levetiracetam (LEV), lamotrigine (LTG), carbamazepine (CBZ), lacosamide (LCM), valproic acid (VPA), ativan (BZD1), klonopin (BZD2), oxcarbazepine (OXC), clobazam (CLB), lacosamide (LCS), zonisamide (ZNS), eslicarbazepine (ESL), phenytoin (PHT), brivaracetam (BRV), anterior temporal lobe (ATL).

nature research

Corresponding author(s): Mark Harnett

Last updated by author(s): Aug 19, 2021

Reporting Summary

Nature Research wishes to improve the reproducibility of the work that we publish. This form provides structure for consistency and transparency in reporting. For further information on Nature Research policies, see our Editorial Policies and the Editorial Policy Checklist.

Statistics

For all statistical analyses, confirm that the following items are present in the figure legend, table legend, main text, or Methods section.

n/a	Confirmed	
☐	☒	The exact sample size (*n*) for each experimental group/condition, given as a discrete number and unit of measurement
☐	☒	A statement on whether measurements were taken from distinct samples or whether the same sample was measured repeatedly
☐	☒	The statistical test(s) used AND whether they are one- or two-sided *Only common tests should be described solely by name; describe more complex techniques in the Methods section.*
☐	☒	A description of all covariates tested
☐	☒	A description of any assumptions or corrections, such as tests of normality and adjustment for multiple comparisons
☐	☒	A full description of the statistical parameters including central tendency (e.g. means) or other basic estimates (e.g. regression coefficient) AND variation (e.g. standard deviation) or associated estimates of uncertainty (e.g. confidence intervals)
☐	☒	For null hypothesis testing, the test statistic (e.g. *F*, *t*, *r*) with confidence intervals, effect sizes, degrees of freedom and *P* value noted *Give P values as exact values whenever suitable.*
☒	☐	For Bayesian analysis, information on the choice of priors and Markov chain Monte Carlo settings
☒	☐	For hierarchical and complex designs, identification of the appropriate level for tests and full reporting of outcomes
☒	☐	Estimates of effect sizes (e.g. Cohen's *d*, Pearson's *r*), indicating how they were calculated

Our web collection on statistics for biologists contains articles on many of the points above.

Software and code

Policy information about availability of computer code

Data collection	Prairie View (Bruker Ultima acquisition software) 5.4 and 5.5
Data analysis	MATLAB 2016a, ImageJ 2016, NEURON 7.8.2

For manuscripts utilizing custom algorithms or software that are central to the research but not yet described in published literature, software must be made available to editors and reviewers. We strongly encourage code deposition in a community repository (e.g. GitHub). See the Nature Research guidelines for submitting code & software for further information.

Data

Policy information about availability of data

All manuscripts must include a data availability statement. This statement should provide the following information, where applicable:

- Accession codes, unique identifiers, or web links for publicly available datasets
- A list of figures that have associated raw data
- A description of any restrictions on data availability

The datasets generated during and/or analysed during the current study are available from the corresponding author on reasonable request.

Field-specific reporting

Please select the one below that is the best fit for your research. If you are not sure, read the appropriate sections before making your selection.

☒ Life sciences ☐ Behavioural & social sciences ☐ Ecological, evolutionary & environmental sciences

For a reference copy of the document with all sections, see nature.com/documents/nr-reporting-summary-flat.pdf

Life sciences study design

All studies must disclose on these points even when the disclosure is negative.

Sample size	No sample size calculation was performed. Sample sizes are comparable or larger than similar studies (Beaulieu-Laroche et al., Cell 2018; Gidon et al., Science 2020, Kalmbach et al, Neuron 2018)
Data exclusions	No datapoints were excluded.
Replication	Findings were not replicated due to the study design. The study consists of >2200 measurements across 22 distinct categories based on subcellular location and species.
Randomization	No randomization was possible as all samples from a given species were analyzed together.
Blinding	There was no blinding as there was no sample allocation.

Reporting for specific materials, systems and methods

We require information from authors about some types of materials, experimental systems and methods used in many studies. Here, indicate whether each material, system or method listed is relevant to your study. If you are not sure if a list item applies to your research, read the appropriate section before selecting a response.

Materials & experimental systems

n/a	Involved in the study
☒	☐ Antibodies
☒	☐ Eukaryotic cell lines
☒	☐ Palaeontology and archaeology
☐	☒ Animals and other organisms
☐	☒ Human research participants
☒	☐ Clinical data
☒	☐ Dual use research of concern

Methods

n/a	Involved in the study
☒	☐ ChIP-seq
☒	☐ Flow cytometry
☒	☐ MRI-based neuroimaging

Animals and other organisms

Policy information about studies involving animals; ARRIVE guidelines recommended for reporting animal research

Laboratory animals	Male Etruscan shrews (suncus etruscus), 3-9 months of age. Male C57BL/6 mice (mus musculus), 12-28 weeks of age. Male mongolian gerbils (meriones unguiculatus), 13-17 weeks of age. Male and female Sprague Dawley rats (rattus norvegius) , 12-32 weeks of age. Female ferrets (mustela putorius furo), 9-16 months of age. Male Hartley guinea pigs (cavia porcellus), 27-32 weeks of age. Male and female New Zealand White rabbits (oryctolagus cuniculus), 25-52 weeks of age. Male and female common marmosets (callithrix jacchus), 2-7 years of age. Male rhesus macaques (macaca mulatta), 8.5-21 years of age.
Wild animals	No wild animals were used in the study
Field-collected samples	No field collected samples were used in the study
Ethics oversight	All animals were used in accordance with NIH where applicable and the Massachusetts Institute of Technology Committee on Animal Care guidelines.

Note that full information on the approval of the study protocol must also be provided in the manuscript.

Human research participants

Policy information about studies involving human research participants

Population characteristics	Male and female patients aged 21-47 years old. Patients underwent brain resections for the reasons listed in Extended Table 3.
Recruitment	Patients were not recruited. Brain tissue was obtained as "discarded tissue" from neurosurgical patients undergoing surgeries for reasons unrelated to this study.
Ethics oversight	Massachusetts General Hospital Internal Review Board & Brigham and Women Internal Review Board

Note that full information on the approval of the study protocol must also be provided in the manuscript.